Progress in Oceanography 149 (2016) 189–213

Contents lists available at ScienceDirect

Progress in Oceanography

journal homepage: www.elsevier.com/locate/pocean

Tidal influence on particulate organic carbon export fluxes around a tall seamount

Robert Turnewitsch [a,*], Matthew Dumont [a,b], Kostas Kiriakoulakis [c], Sonya Legg [d], Christian Mohn [e], Florian Peine [f], George Wolff [g]

[a] Scottish Association for Marine Science, Oban PA37 1QA, UK
[b] University of Edinburgh, School of Geosciences, Grant Institute, The King's Buildings, James Hutton Road, Edinburgh EH9 3FE, UK
[c] Liverpool John Moores University, Byrom St., Liverpool L3 3AF, UK
[d] Princeton University, Atmospheric and Oceanic Sciences, 300 Forrestal Road, Sayre Hall, Princeton, NJ 08544, USA
[e] Aarhus University, Department of Bioscience - Applied Marine Ecology and Modelling, Frederiksborgvej 399, 4000 Roskilde, Denmark
[f] University of Rostock, Institute for Biosciences – Marine Biology, Albert-Einstein-St. 3, 18059 Rostock, Germany
[g] University of Liverpool, Department of Earth & Ocean Sciences, Liverpool L69 3GP, UK

ARTICLE INFO

Article history:
Received 8 April 2016
Received in revised form 19 October 2016
Accepted 19 October 2016
Available online 1 November 2016

Keywords:
Seamount
Tide
Particulate organic carbon export
Cape Verde

ABSTRACT

As tall seamounts may be 'stepping stones' for dispersion and migration of deep open ocean fauna, an improved understanding of the productivity at and food supply to such systems needs to be formed. Here, the $^{234}Th/^{238}U$ approach for tracing settling particulate matter was applied to Senghor Seamount – a tall sub-marine mountain near the tropical Cape Verde archipelago – in order to elucidate the effects of topographically-influenced physical flow regimes on the export flux of particulate organic carbon (POC) from the near-surface (topmost $\leqslant$ 100 m) into deeper waters. The comparison of a suitable reference site and the seamount sites revealed that POC export at the seamount sites was ~2–4 times higher than at the reference site. For three out of five seamount sites, the calculated POC export fluxes are likely to be underestimates. If this is taken into account, it can be concluded that POC export fluxes increase while the passing waters are advected around and over the seamount, with the highest export fluxes occurring on the downstream side of the seamount. This supports the view that biogeochemical and biological effects of tall seamounts in surface-ocean waters might be strongest at some downstream distance from, rather than centred around, the seamount summit. Based on measured (vessel-mounted ADCP) and modelled (regional flow field: AVISO; internal tides at Senghor: MITgcm) flow dynamics, it is proposed that tidally generated internal waves result in a 'screen' of increased rates of energy dissipation that runs across the seamount and leads to a combination of two factors that caused the increased POC export above the seamount: (1) sudden increased upward transport of nutrients into the euphotic zone, driving brief pulses of primary production of new particulate matter, followed by the particles' export into deeper waters; and (2) pulses of increased shear-driven aggregation of smaller, slower-settling into larger, faster-settling particles. This study shows that, under certain conditions, there can be an effect of a tall seamount on aspects of surface-ocean biogeochemistry, with tidal dynamics playing a prominent role. It is speculated that these effects can control the spatiotemporal distribution of magnitude and nutritional quality of the flux of food particles to the benthic and benthic-pelagic communities at and near tall seamounts.

1. Introduction

A fraction of the biogenic particulate matter that is photoautotrophically produced in the upper sunlit layers of the ocean settles into deeper waters and constitutes food for heterotrophic organisms in the deeper waters and the seafloor. Often this downward 'export' of biogenic particulate matter from the topmost 10 s or 100 s of meters of the water column is quantified in terms of the export of particulate organic carbon (POC). On large quasi-horizontal scales on the order of 1000 s of kilometers, the combination of basin-scale current distribution and latitudinally dependent insolation indirectly control the distribution of primary productivity and POC export (e.g., Lutz et al., 2007; Watling et al., 2013). On

* Corresponding author.
E-mail address: robert.turnewitsch@sams.ac.uk (R. Turnewitsch).

http://dx.doi.org/10.1016/j.pocean.2016.10.009
0079-6611/

quasi-horizontal scales on the order of 10–100 s of kilometers, physical-oceanographic features such as mesoscale eddies and fronts are known to influence POC export (e.g., Buesseler et al., 2008; Resplandy et al., 2012). Islands and island chains have also been shown to effects POC export through their effects on regional and local flow dynamics (e.g., Bidigare et al., 2003; Morris et al., 2007; Maiti et al., 2008; Verdeny et al., 2008). By contrast, very little is known about the influence of submarine mountains. Seamounts are often defined as tall (>1000 m from base to summit), relatively isolated submarine features, of which there are estimated to be well over 100,000 across the ocean (Wessel et al., 2010). About 2000 seamounts are thought to be at least 3000 m high, with the vast majority reaching water depths of $\leqslant$100 m.

Seamounts interact in systematic and complex ways with different flow components of ocean currents, including quasi-steady and oscillating ones (see, for example, reviews by White and Mohn, 2004; Lavelle and Mohn, 2010; Turnewitsch et al., 2013). As tall seamounts may be 'stepping stones' for dispersion and migration of deep open ocean fauna (Rowden et al., 2010), an improved understanding of the productivity and food supply to such systems needs to be formed. It has been argued that the fluid dynamics at seamounts that reach into the near-surface ocean could have a significant effect on local or regional water column biogeochemistry (Goldner and Chapman, 1997; Mullineau and Mills, 1997; Mohn and White, 2010). This could lead to seamounts acting as hotspots of high productivity and potentially high POC-export, at least in oligotrophic regions, a phenomenon described as the 'seamount'- or 'classic'- hypothesis (Dower and Mackas, 1996). Observed enhancements of primary production around seamounts have been attributed to a greater local upward mixing of deep, nutrient-replete waters (Rogers, 1994; Mouriño et al., 2001). However, as noted by Genin (2004), upwelling is unlikely to be a permanent feature and any enhancement of primary production might only be realised downstream of the seamount. Rowden et al. (2010) also argue that the paradigm that tall seamounts "have high production supported by localised bottom-up forcing, [is] not supported by the weight of existing evidence".

This paper presents the first case study in which the distribution of export of POC from the surface waters near and over a tall seamount was investigated. For the particular situation at the time of the study, the three main objectives were (O1) to identify the predominant physical-oceanographic features at and near the seamount; (O2) to establish how POC export is distributed at the seamount compared to reference stations; and (O3) to scrutinize the results of O1 and O2 for a seamount effect on POC export. The core hypothesis is that a tall seamount can trigger enhanced localised POC export. The findings of this study illustrate the importance of the physical-oceanographic complexity that results from regional 'background' variability and seamount-controlled flow/topography interactions for an understanding of biogeochemical processes at tall seamounts. The results indicate that, in the case of Senghor Seamount, tidally generated internal waves are likely to have led to an abrupt and localised enhancement of POC export, with this biogeochemical signal being advected downstream and away from the seamount.

2. Material and methods

2.1. Environmental setting

The study was carried out at Senghor Seamount, a large, approximately conical feature on the Cape Verde Rise, centred at ~17.2°N, 21.9°W and ~110 km north-east of Sal Island of the Cape Verde archipelago and ~550 km west of the coast of Senegal (Fig. 1). The summit plateau is at ~105 m depth whereas the rise is at ~3200 m. The summit plateau has a maximum extent of ~5 km; at the base the seamount has an approximate diameter of 35 km. The seamount is situated amongst several well-studied oceanographic features, including the Cape Verde Frontal Zone (CVFZ; Zenk et al., 1991) to the north (N) and northwest (NW) (Fig. 1), the Mauritanian Upwelling Zone (Mittelstaedt, 1983) to the northeast (NE), and the Guinea Dome (Siedler and Zangenberg, 1992) and Shadow Zone (Luyten et al., 1983) to the south (S).

Current-flow data derived from nearby moorings (Müller and Siedler, 1992; Vangriesheim et al., 2003), Acoustic Doppler Current Profiler (ADCP) transects (Stramma et al., 2008), and satellite-altimetry-forced models (Lázaro et al., 2005) suggest that at depths shallower than ~800 m mean residual flow in the region is to the southwest (SW) at ~0.05–0.1 m s^{-1} which is consistent with the general direction of the North Equatorial Current (NEC) (Fig. 1). At depths greater than ~800 m, residual flow is to the south at only 0.005–0.01 m s^{-1}. Important sources of variability that are superimposed onto this mean residual flow are the seasonal migration of the wind-stress curl with the inter-tropical convergence zone (ITCZ) (Stramma and Siedler, 1988; Lázaro et al., 2005), baroclinic instabilities originating from the CVFZ), barotropic tidal oscillations (Siedler and Paul, 1991), and internal (baroclinic) tides (Siedler and Paul, 1991; Arbic et al., 2012).

Although the centre of the Mauritanian Upwelling Zone is located off Cape Blanc, i.e., well to the NE of Senghor Seamount, filaments of upwelled water have been observed to extend out westward driven by trade-winds and meso-scale eddies (Mittelstaedt, 1983; Pastor et al., 2008; Meunier et al., 2012). The filaments tend not to extend southward towards Senghor Seamount though. Nevertheless, satellite remote sensing data from MODIS-Aqua (acquired from giovanni.gsgc.nasa.gov) will be utilised to evaluate the extent of eutrophic waters during this study.

Primary production typically peaks in the first quarter of the year, following the wind stress maximum (Lathuilière et al., 2008; Ohde and Siegel, 2010); but spatially- and temporally-sporadic peaks in productivity have been observed later between April and June, and it has been speculated that they occur in association with dust deposition from the Sahara and Sahel regions (Ratmeyer et al., 1999b; Fitzsimmons et al., 2013). However, dust deposition in summer has been noted to be five-times lower than in December and January (Chiapello and Bergametti, 1995); and, using a remotely sensed optical aerosol depth index and chlorophyll-*a* concentration as proxies for dust deposition and productivity, respectively, Ohde and Siegel (2010) reported that the input of Saharan dust accounts for just 5% of the variability in observed chlorophyll-*a* concentrations. By contrast, there is some evidence to suggest that large amounts of dust particles that are incorporated into marine-snow aggregates could lead to increased mass densities of these aggregates and, as a consequence, higher settling speeds and POC export (e.g., Fischer et al., 2016).

2.2. The $^{234}Th/^{238}U$ approach to estimate POC export

The use of the thorium-234/uranium-238 ($^{234}Th/^{238}U$) pair of naturally occurring radionuclides to measure export flux is made possible due to the contrasting adsorption behaviours of the two elements (Bhat et al., 1968; Coale and Bruland, 1985, 1987; Buesseler, 1998). In oxygenated seawater the very long-lived ^{238}U (half life: $t_{1/2} \approx 4.468$ billion years) behaves chemically conservative and is removed only by alpha-decay to its daughter, ^{234}Th. If unperturbed, the two radionuclides remain in so-called radioactive equilibrium: i.e., over negligibly-short time scales relative to the half-life of ^{238}U, the rate of decay of ^{234}Th is matched by the rate of decay of ^{238}U. However, in seawater Th is highly particle reactive (e.g., Santschi et al., 2006) and readily scavenged by

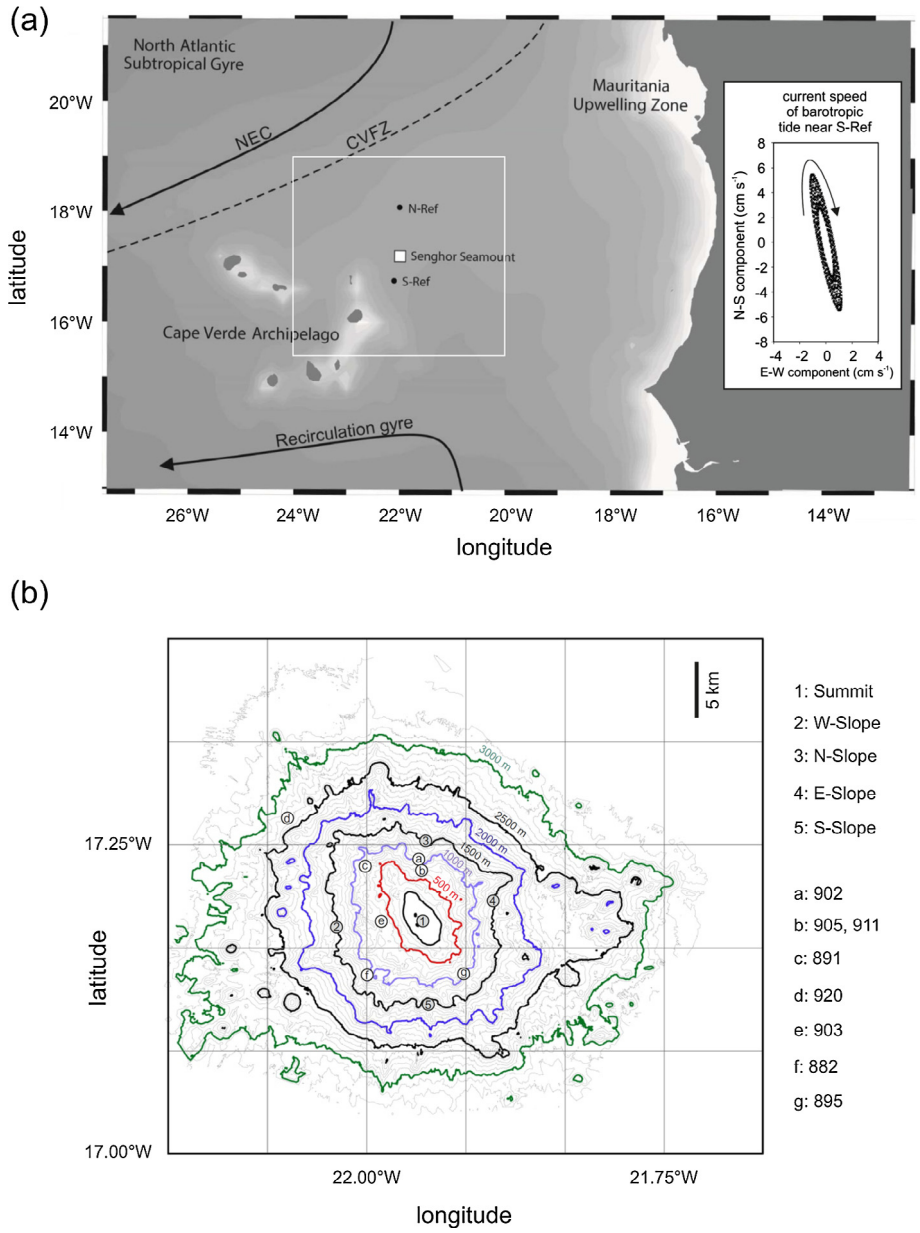

Fig. 1. (a) Map of the wider study area. NEC: North Equatorial Current; CVFZ: Cape Verde Frontal Zone. N-Ref: northern reference (far-field) site; S-Ref: southern reference (far-field) site. White box: location of Senghor Seamount. White rectangle line: area for which the near-surface currents are shown in Fig. 2a and b. Inset: ellipse of the clockwise-rotating current vector of the barotropic tide near S-Ref for the duration of the cruise, capturing two spring and two neap tides (extracted with hourly resolution from the TPXO barotropic tide model; Egbert and Erofeeva, 2002). (b) Swath-bathymetric map of Senghor Seamount. Grey circles and numbers: ^{234}Th sampling; white circles and letters: only hydrography.

adsorption onto particle surfaces, with an affinity for acid polysaccharides (Guo et al., 2002; Alvarado Quiroz et al., 2006; Buesseler et al., 2006). Most research so far suggests that larger, more rapidly-settling particles play the dominant role in the export of POC into the *deep interior* ocean (e.g. McCave, 1975; Clegg and Whitfield, 1990,1991; Ducklow et al., 2001; De La Rocha and Passow, 2007) (in the topmost few hundred meters of the water column smaller slowly-settling particles can also contribute significantly to the downward flux of particulate matter, but only into the shallower twilight zone; e.g., Alonso-González et al., 2010). On these settling particles, the adsorbed ^{234}Th is transported downwards and 'exported' from its original parcel of water. If the rates of adsorption and settling are high in comparison to the production rate of ^{234}Th, a radioactive disequilibrium between ^{238}U and ^{234}Th forms, i.e., the radioactivity of ^{238}U is higher than the radioactivity of ^{234}Th. This disequilibrium can be used as a measure of the intensity of the export flux of ^{234}Th from a given parcel of water. If the ratio of POC to ^{234}Th is known for the settling particles, the ^{234}Th export flux can be converted into a POC export flux. Due to the short half-life of ^{234}Th ($t_{1/2}$ = 24.1 d) it captures the characteristic time scales of many bio-oceanographic processes such as phytoplankton blooms (Buesseler et al., 2006; Passow et al., 2006).

2.2.1. Sampling

Samples were collected during cruise M79/3 of R/V Meteor (24/09-22/10/2009; Christiansen et al., 2011). A map of sampling sites around the seamount along with two additional far-field stations north (N-Ref) and south (S-Ref) of the seamount is shown in Fig. 1. Water samples for total (dissolved + particulate) ^{234}Th were collected with a 22-bottle Seabird-Systems CTD-rosette

(SBE 911plus) equipped with a Winkler-calibrated dissolved-oxygen (DO) probe. Within the topmost 100 m 5–8 depths were sampled for total ^{234}Th (S-Slope: 5 depth levels; Summit, W-Slope, N-Slope, E-Slope, S-Ref: 6 depth levels; N-Ref: 8 depth levels) (Table 1).

To collect samples for POC and ^{234}Th in particulate matter, up to two large-volume stand-alone pumping systems (SAPS; Challenger Oceanic) were deployed at the aforementioned CTD stations (Table 1). The SAPS filtered between 381 and 1634 L of water through a 293 mm-diameter, acid-washed 53 μm nylon mesh before two sequentially-stacked pre-ashed glass fibre GF/F filters with a nominal pore-size of 0.7 μm. The second GF/F filter was used to correct for what is thought to be adsorption of dissolved organic carbon (DOC) (Turnewitsch et al., 2007) and dissolved ^{234}Th onto the GF/F filters. Material collected on the mesh and the filters was analysed for organic carbon and ^{234}Th (see Section 2.2.2 below). This approach thus differentiated POC and ^{234}Th in operationally defined nominal particle-size fractions of 0.7–53 μm and >53 μm.

2.2.2. Laboratory and analytical procedures

2.2.2.1. Total ^{234}Th. Total ^{234}Th analysis was carried out on the bottle-collected water samples, applying the procedures outlined by Rutgers van der Loeff and Moore (1999), Turnewitsch and Springer (2001) and Turnewitsch et al. (2008) with slight modifications and taking into account the review of Rutgers van der Loeff et al. (2006). Sample processing involved co-precipitating thorium in the unfiltered samples with MnO_2. To form MnO_2, 150 μL of 25% NH_3 solution, 100 μL of $KMnO_4$ solution (60 g L^{-1}) and 40 μL of $MnCl_2{\cdot}4H_2O$ solution (400 g L^{-1}) were added successively to each sample. The processed water volume was of intermediate size for this kind of analysis (average ± one standard deviation (1SD): 7.772 ± 0.716 L). The precipitating MnO_2 particles were left to grow for between ~6 and ~12 h. The MnO_2-containing water was then filtered at 400 mbar overpressure through 142-mm-diameter polycarbonate filters with 1.0 μm nominal pore width to collect the precipitate and natural particles. This step of the procedure separates thorium from its dissolved uranium parent. Following filtration, the polycarbonate filters were air dried, folded in a reproducible way, and wrapped in Mylar foil before being placed into a beta counter.

Beta counting was performed using three identical Risø GM25-5A multicounters: one aboard R/V Meteor, one at the University of Rostock and another at the Scottish Association for Marine Science (SAMS). Each betacounter has 5 detectors and the 15 detectors that were used were intercalibrated with standard filters that carry a known ^{238}U radioactivity in equilibrium with ^{234}Th (Turnewitsch and Springer, 2001; Turnewitsch et al., 2008). This intercalibration also yielded the counting efficiencies for the 15 detectors. Counting efficiencies ranged from 28% up to 33% with absolute errors (given as 1SD) ranging from ±1% to ±1.74%. Each sample was measured on board as soon as possible after sample processing and then again at least three times over a period of ten months (approximately twelve ^{234}Th half-lives). Repeat measurements ensure that the shape of the decay curve can be scrutinised for signs of contamination (Peine et al., 2009) and that a robust background can be determined. Mean ± 1SD background activities were 0.50 ± 0.12 counts per minute (cpm).

To estimate total ^{234}Th activities (expressed as disintegrations per minute (dpm) per litre of in situ seawater: dpm L^{-1}) a correction for in-growth from ^{238}U decay between sampling and filtration was applied. Another correction includes the decay-related loss of ^{234}Th between filtration and the first activity measurement. ^{238}U activities in dpm L^{-1} were derived from the relationship with salinity as described by Chen et al. (1986) and re-evaluated by Owens et al. (2011). Overall uncertainties for total ^{234}Th activities are reported as ±1SD and resulted from error propagations, taking into account uncertainties in in situ mass density of sampled waters, intercalibration, counting statistics, estimate of the activity at the time of sampling (corrections for ^{234}Th decay and ingrowth), counting efficiency, filtered volume, and ^{238}U activity (Turnewitsch et al., 2008).

On previous cruises, a second precipitation was conducted on selected samples to directly determine the extraction efficiency,

Table 1
Sampling-site locations, sampling devices, and sampling depths. SAPS: large-volume Stand-Alone Pumping System.

Site	Station	Latitude (°N)	Longitude (°W)	Water depth at seafloor (m)	Sampling device	Sampling depths (m)
Northern reference (*N-Ref*)	801	18.0858	21.9998	3295	Bottles	15, 25, 200
	803	18.0828	21.9993	3295	SAPS	150
	808	18.0838	22.0007	3295	Bottles	5, 60, 100
					SAPS	32[a]
	812	18.0820	22.0015	3295	Bottles	35, 1400[b]
	813	18.0833	21.9998	3295	Bottles	45, 75, 150
Northern slope (*N-Slope*)	885	17.2533	21.9503	1575	SAPS	150
	1020	17.2532	21.9512	1555	Bottles	5, 15, 25, 45, 75, 100, 200
	1039	17.2533	21.9508	1570	SAPS	50
Summit (*Summit*)	840	17.1883	21.9533	100	Bottles	5, 15, 25, 45, 75, 95
					SAPS	50, 90
Western slope (*W-Slope*)	875	17.1833	22.0267	1520	SAPS	150
	1001	17.1840	22.0270	1535	Bottles	5, 15, 25, 45, 75, 100, 200
	1002	17.1840	22.0270	1535	SAPS	50
Eastern slope (*E-Slope*)	858	17.2050	21.8933	1550	SAPS	150
	1028	17.2045	21.8948	1485	Bottles	5, 15, 25, 45, 75, 100, 200
	1029	17.2047	21.8947	1500	SAPS	50
Southern slope (*S-Slope*)	896	17.1212	21.9482	1635	SAPS	150
	998	17.1212	21.9490	1645	Bottles	5, 249
	999	17.1210	21.9488	1640	Bottles	15, 45, 75, 100
					SAPS	50
Southern reference (*S-Ref*)	1048	16.7502	22.1005	3375	Bottles	5, 15, 25, 45, 75, 100, 200
					SAPS	50, 150

[a] SAPS cast accidentally hoisted up from 50 m to 15 m during pumping. Sampling depth given as mid-point (32 m).
[b] Station, site and depth for replicate sampling.

and, for total ^{234}Th, extraction efficiencies were found to be 99.0 ± 1.4% which is analytically indistinguishable from the 98 ± 3% reported independently by Le Moigne et al. (2013). There is growing evidence that even waters from the interior ocean (i.e., away from ocean boundaries) may contain detectable disequilibria (e.g., Owens et al., 2015). However, replicate sampling (N = 5) at ~1400 m water depth (1894 m above bottom (mab)) at N-Ref revealed an average ± 1SD total ^{234}Th activity of 2.37 ± 0.13 dpm L^{-1} (relative uncertainty of ±5.5%) which is analytically indistinguishable from the salinity-derived ^{238}U activity of 2.44 ± 0.05 dpm L^{-1} and indicates the ^{234}Th/^{238}U pair was in fact in radioactive equilibrium at this location and depth. This demonstrates within analytical uncertainties the quantitative recovery of thorium from the seawater samples for this intermediate-volume technique and is in agreement with a number of previous studies (e.g., Morris et al., 2007; Lampitt et al., 2008; Turnewitsch et al., 2008; Le Moigne et al., 2013).

2.2.2.2. Particulate ^{234}Th, particulate organic carbon (POC) and particulate nitrogen (PN). For particulate ^{234}Th, SAPS samples were processed following the approach described by Morris et al. (2007), with slight modifications. For POC and PN, procedures followed Turnewitsch et al. (2007), with slight modifications. In summary, particles collected on the 53 μm nylon mesh were rinsed with purified water into a graduated cylinder. The sample was then gently stirred to homogenise the particles in suspension. While still swirling, the suspension was split: one split of known volume was immediately filtered onto 25 mm diameter pre-ashed GF/F filters that were then stored frozen until POC and PN analysis; the other split of known volume was immediately filtered through a 0.4 μm nominal pore width 142 mm-diameter polycarbonate filter that was air-dried, folded and wrapped in Mylar foil in a reproducible manner for particulate ^{234}Th analysis. Exposure of the particles to the purified water was limited to a few minutes. For the smaller particle size fraction (0.7–53 μm), four 24 mm diameter disk subsamples were taken from each of the 293 mm diameter pre-ashed GF/F filters which were then air-dried in preparation for direct beta-counting as described above. Corresponding GF/F-filter subsamples for POC and PN were stored frozen for later analysis.

Counting efficiencies for the folded polycarbonate filters that carry the >53 μm particles were determined with standard filters as described above. As the GF/F filter sub-samples have similar mass density and diameter (and thus similar absorption properties) compared to the QMA-filter sub-samples that we used as part of the GEOTRACES ^{234}Th intercalibration (Maiti et al., 2012), the counting efficiency of 43 ± 2% that was determined for the QMA filter disks was applied to the filter sub-samples of this study. Activities on the first GF/F filter were corrected based on activities on the second GF/F filter, assuming that activities on the second filter represent the combination of activity due to ^{234}Th that adsorbed from the dissolved phase onto the filter and activity from the background of comparatively long-lived beta-emitters (Benitez-Nelson et al., 2001). Activities were corrected for ^{234}Th decay between sampling and the first measurement.

The analytical method to determine POC and PN was similar to that performed by Kiriakoulakis et al. (2009). In short, SAPS filter sub-samples for both particle size fractions were decarbonated for POC analysis (Yamamouro and Kayanne, 1995), whilst PN analysis was carried out on non-decarbonated subsamples. Analysis was then carried out using a CEInstruments NC 2500 CHN analyser with quadruplicates. Adsorption of dissolved organic matter (DOM) onto the GF/F filters was corrected for by subtracting the values obtained for the second in-line filter from values that were obtained for the first filter (Turnewitsch et al., 2007).

Calculations of final particulate-^{234}Th activity and final POC and PN concentrations took into account corrections for the split volume and scaling-up to full effective filter areas of the 293 mm-diameter filters and filtered volumes.

2.3. Physical oceanography

Information on hydrography and flow dynamics around the upper parts of the seamount was derived from the CTD casts, vessel-mounted ADCP (VM-ADCP) measurements and numerical modelling. Due to a technical defect, CTD data from stations with station numbers higher than 911 (with the exception of 920 and 951) are incomplete or not readable. Water samples could still be collected reliably though. On-station and underway VM-ADCP data were collected across Senghor Seamount with a 38-kHz Teledyne RD Instruments Ocean Surveyor system mounted in the ship's hull (see ship tracks in Fig. S1, Online Supplement). Single ping velocity profiles (60 bins) were sampled, each bin with a vertical length of 16 m (first bin at 30 m) and a maximum sampling depth of 974 m. Additional VM-ADCP data were obtained during cruise 446 of RV Poseidon in February 2013 with a 75-kHz Ocean Surveyor. Here, an 8 m bin length was used and data are available from 24 m downwards.

Time-averaged (2 min) ensembles of velocity profiles (RDI Ocean Surveyor raw data format including basic error screening and navigation) were used for data processing with the Common Oceanographic Data Access System (CODAS) (Firing et al., 1995; http://currents.soest.hawaii.edu/docs/adcp_doc/index.html). Processing steps followed the recommendations by Hummon and Firing (2003) and are described in detail by Mohn et al. (2013), including horizontal re-gridding using DIVA (Data Interpolating Variational Analysis; Troupin et al., 2012). Error plots are provided in Fig. S1 in the Online Supplement. Additional information on the horizontal advective flow field in the wider region during (October 2009) and just before (September 2009) the field study was derived from AVISO altimetry, resolving mesoscale variability.

To acquire a better picture of the interaction of barotropic (surface) tides with Senghor seamount, simulations were performed using the non-hydrostatic MITgcm (Marshall et al., 1997) in a two-dimensional (2D) configuration similarly employed by Legg and Huijts (2006) and Legg and Klymak (2008). Simulations were forced by a barotropic N-S flow of the predominant tidal M_2 constituent at a velocity amplitude of 5 cm s^{-1}, corresponding to the approximate maximum during spring tides in the region (Egbert and Erofeeva, 2002). The N-S section was chosen as it is expected that the strongest internal tides will propagate in the direction of the major axis of the dominant barotropic M_2 constituent, which is aligned approximately N-S in the region (Siedler and Paul, 1991; Egbert and Erofeeva, 2002; Fig. 1a). The UNESCO equation of state is used and the barotropic flow is forced by a body forcing term in the momentum equation. The simulation was run for 3.5 M_2 tidal cycles.

The simulations had realistic initial mass-density stratification with initial temperature and salinity profiles taken from station 812 at N-Ref and smoothed over 20 m vertical bins. Realistic swath-bathymetry was used along the N-S section across the seamount at a longitude of 21.95°W (averaging over 0.05 degrees in the longitudinal direction to smooth out some of the local topography). The seamount summit was at the centre of the model domain, with a large region on either side with a uniform depth of 3200 m. The total domain size is 300 km across and 3200 m deep, with a total number of 2000 horizontal grid points and 300 vertical grid points. Horizontal resolution is higher nearer the seamount, where Δx = 55 m, increasing to Δx = 1 km away from the topography. In the vertical, resolution is highest in the upper 500 m, where Δz = 2 m, and Δz increases to 49 m at depth. No-slip boundary conditions are applied at the topography. At the

sides, a radiative boundary condition is applied to the baroclinic flow to allow waves to propagate out of the domain.

It has to be stressed that the 2D arrangement of these simulations tends to produce unrealistically high absolute current speeds of the baroclinic (internal) tides, unrealistically high rates of kinetic energy dissipation and vertically exaggerated responses, such as displacement of isotherms. Nevertheless, the simulations can be used to demonstrate *where* tides may alter rates of dissipation of turbulent kinetic energy and vertical mixing around the seamount.

3. Results and discussion

Before results for ^{234}Th, POC, PN and export can be discussed the physical-oceanographic context needs to be scrutinised to clarify which fluid-dynamic features are of most relevance to this study. This physical-oceanographic context will, therefore, be developed in Section 3.1. The results for ^{234}Th, for POC and PN, and for POC export will then be presented and discussed in Sections 3.2, 3.3 and 3.4, respectively.

3.1. Physical oceanography

3.1.1. Larger-scale regional flow features

The location of the 36 isohaline at 150 m depth is considered an indicator for the proximity of the CVFZ in the region (Zenk et al., 1991; Martínez-Marrero et al., 2008). In this study we observed the 36 isohaline at between 50 m and 75 m depth at all stations, too shallow to indicate the presence of the CVFZ at Senghor Seamount. Over the long-term, satellite-altimetry-derived average distribution of the surface currents in the wider study region also suggests that the CVFZ rarely reaches Senghor Seamount (Lázaro et al., 2005). Moreover, a time series of remotely sensed regional chlorophyll-*a* distribution in the surface waters shows no evidence of the CVFZ having been anywhere near the seamount or having shed eddies that may have interfered with the processes at the seamount in the ~3 months before the cruise and during the cruise (see Fig. S2 in the Online Supplement). The chlorophyll time series also shows that, at the seamount and S-Ref, there were no filaments or eddies shed away from the Mauritanian upwelling during the cruise and during the ~3 months before the cruise. However, in October 2009 N-Ref happened to be near the southwestern side of a mesoscale eddy that was associated with high chlorophyll concentrations (Fig. S2). In Section 3.1.3 it will be argued that this was close enough to affect the fluid and particle dynamics at N-Ref, questioning its suitability as a reference station for the seamount sites.

3.1.2. Interaction of 'background' flow with the seamount

In the study area, background flow consists of the flow components of mesoscale eddies and the quasi-steady 'residual' flow of the basin-scale circulation. A comparison of the AVISO-derived flow field in September 2009 (Fig. 2a) with the flow field in October 2009 (Fig. 2b) reveals that Senghor Seamount was situated amongst mesoscale eddies, with these eddies slowly migrating westwards at a residual background speed of ~4 cm s^{-1}. In October, when the vast majority of the samples was collected, there were three mesoscale eddy features: (1) one fairly circular and strongly clockwise-rotating eddy centred around about 18.7°N, 20.7°W, i.e., ~220 km to the NE of Senghor Seamount; (2) one also fairly circular and strongly clockwise-rotating eddy centred about 16.5°N, 20.0°W, i.e., ~220 km to the SE of Senghor Seamount; and (3) an elongated weakly anticlockwise-rotating eddy that reached from about 18.0°N, 24.0°W to about 17.0°N, 21.5°W. That is, while sampling was carried out at Senghor, the seamount happened to be located at the ESE end of the elongated weakly anticlockwise-rotating eddy. Comparison of the AVISO-derived regional flow field (Fig. 2b) with the VM-ADCP-derived composite pictures of the flow field at Senghor (Fig. 3) reveals that, just south of the seamount, surface currents were still flowing eastward; just east of the seamount they were turning northward; and to the NE of the seamount they were then turning back and onto the seamount, leading to the surface waters to impinge on the upper seamount from the NE at current speeds of around ~10 cm s^{-1}. This smaller seamount-scale flow vorticity is not resolved by the AVISO map. Maps of remotely-sensed chlorophyll *a* and net primary productivity (NPP) as derived from the Vertically Generalized Productivity Model (VGPM; Behrenfeld and Falkowski, 1997) show that the two clockwise-rotating eddies were sufficiently far from Senghor Seamount so that they had no direct influence on the processes at the seamount (Fig. 2c and d). VM-ADCP data show that the eddies reached no deeper than ~150–200 m (Figs. 5 and 6).

During this study NPP was consistently low near and south of the seamount and indicates tropical non-bloom conditions (Maiti et al., 2008). It also appears that S-Ref has been lying in the same type of low-NPP waters that then turned back onto and impinged on the seamount from the NE. By contrast, the wider regional flow field also shows that N-Ref was situated in an area of a strong SW-NE gradient of horizontal current speeds between the anticlockwise eddy and the clockwise northeastern eddy. This means N-Ref is likely to have been affected by horizontal turbulence intensities that were higher than at the other sampling sites of this study. Overall, these circumstances render S-Ref a more suitable reference for the seamount sites than N-Ref.

The ADCP data revealed that between ~250 m and at least ~600 m (the latter not shown), the background flow was approximately 5 cm s^{-1} to the SSW (Fig. 3), similar to the time-mean flow velocities observed during other studies in this region (Müller and Siedler, 1992; Vangriesheim et al., 2003). There is also interesting evidence for clockwise (looking from above) recirculation around the seamount near the seafloor, with current speeds of comparable magnitude to the background flow between ~400 m and at least ~600 m depth (the latter not shown) (Fig. 3). As far as the background flow is concerned, this recirculation constitutes the main distinction between the topmost ~250 m and the deeper layers of the upper water column above the seamount. This deeper recirculation may have been part of a weak Taylor column (Chapman and Haidvogel, 1992) or due to weak tidal rectification (Goldner and Chapman, 1997).

If there was a weak Taylor column, then its vertical extent was limited to waters deeper than ~250 m. This limitation may be due to the strong mass-density stratification in the topmost ~100 m. Composite hydrographic N-S and E-W sections exhibited evidence of isohaline, isotherm and oxygen-isopleth doming towards the summit in the upper ~150 m of the water column (see Fig. 9). Doming was also observed by Hanel et al. (2010) in April 2005. The doming of isopleths within the topmost ~100 m above and around the summit is, therefore, most likely simply due to somewhat deeper waters being forced up and over the summit plateau while the advected waters pass the seamount rather than due to recirculation around the seamount. Overall, the ADCP and hydrographic results indicate that surface waters (the topmost ~200 m) were not trapped at the seamount. Consequently, trapping of nutrients and/or particles at the seamount are very unlikely to have played a significant role for pelagic productivity and particle export from the surface ocean during this study.

Finally, it needs to be stressed that there is the possibility that advection of waters past the upper parts of a tall seamount can lead to localised order-of-magnitude enhancement of dissipation of kinetic energy and resulting turbulent mixing (Gibson et al., 1993), with a potential influence on nutrient redistribution and/or particle dynamics at and downstream of the upper seamount.

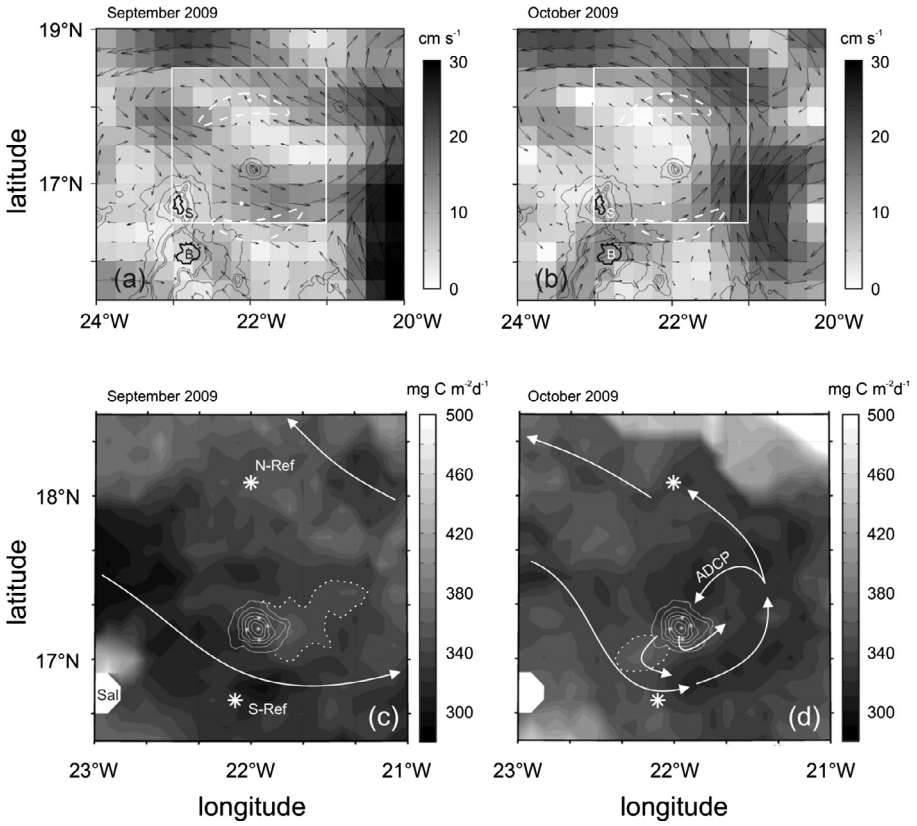

Fig. 2. (a) AVISO-derived surface currents during September 2009. Bold isobaths: outlines of Sal island (S) and Boa Vista island (B). Areas surrounded by dashed white lines: approximate regions where the initial downward semidiurnal internal-tide beams that are generated on the upper slopes of Senghor Seamount reflect from the sea surface (also see Fig. S3). White circles: locations of N-Ref and S-Ref. Area surrounded by white rectangle line: area shown in (c) and (d). (b) Same as (a), but for October 2009. (c) Map of net primary productivity (NPP) in September 2009 as derived from the Vertically Generalized Productivity Model (VGPM; Behrenfeld and Falkowski, 1997). White approximately concentric lines: approximate outline of Senghor Seamount. White star symbols: sampling sites. White arrows: approximate (hand-drawn) AVISO-derived surface currents. The area that is surrounded by a thin white dashed line and emanates from the seamount indicates what could be a 'banner cloud' of seamount-enhanced NPP on the downstream side of the seamount. (d) Same as (c), but for October 2009. The detail of the approximate hand-drawn currents labelled 'ADCP' is derived from the VM-ADCP survey as shown in Fig. 3.

As we have no direct measurements of kinetic energy dissipation, this has to remain a speculative possibility at this point.

3.1.3. Interactions of tides with the seamount

In addition to the lower-frequency background flow, other key flow components that could have played a role are higher-frequency tidal and near-inertial ones (Garrett and Kunze, 2007; Alford et al., 2016). VM-ADCP data for the topmost ~1000 m indicate that there can be near-intertial oscillations at Senghor Seamount (Fig. 4a). At a latitude of ~17°, near-inertial oscillations have a period of ~40 h. The observed oscillations had a predominant E-W component and were more obvious during the first half of the ship time at Senghor. These internal waves phase-propagated downwards, indicating an energy source at depth and probably being a result of the interactions of variable currents with the seamount.

In contrast to the near-inertial oscillations tidal oscillations are continuous and therefore probably more important for nutrient redistribution and/or particle dynamics. Near Senghor in the far field, the TPXO barotropic-tide model of Egbert and Erofeeva (2002) predicts the ellipse of the current vector of the predominantly semidiurnal barotropic tide to be strongly elongated in the NNW and SSE direction (Fig. 1a). The NNW-SSE predominance in semidiurnal oscillations is clearly reflected in the VM-ADCP time series obtained at Senghor Seamount in October 2009 (Fig. 4a).

The flow components of the barotropic (surface) tide may push water partly over the summit, potentially contributing to isopleth doming and leading to flow acceleration on and near the summit plateau. Furthermore, when mass-density-stratified waters are forced over a topographic obstacle by barotropic tides, internal gravity waves of tidal frequency (internal or baroclinic tides) are generated (Garrett and Kunze, 2007). For topographic obstacles equatorwards of specific critical latitudes, these internal tides can propagate away from their generation sites; by contrast, polewards of the critical latitudes, internal tides are trapped at their generation sites. For diurnal and semidiurnal tides, the critical latitudes are ~30° and ~74.5°, respectively. Senghor is equatorwards of these critical latitudes and it is therefore very safe to assume that trapped internal tidal waves do not occur at Senghor Seamount. Hence, internal tides that are formed at Senghor propagate away from their generation sites. Because of the NNW-SSE predominance of the barotropic tidal forcing it can be assumed that the strongest propagating internal tides occur on the NNW and SSE sides of the seamount, as indicated by the dashed lines in Fig. 3.

The MITgcm simulations show that the predominant semidiurnal barotropic tide that interacts with Senghor Seamount leads to the generation of internal-tide beams near the summit of the seamount. In Fig. 4b, the approximate paths of initially upward and downward beams are indicated by thin black and white lines, respectively. The upward beams reflect downwards from the sea surface around 15 km north and south of the centre of the summit plateau. The beam areas are associated with intensified dissipation of kinetic energy, especially in the upper ocean near the seamount

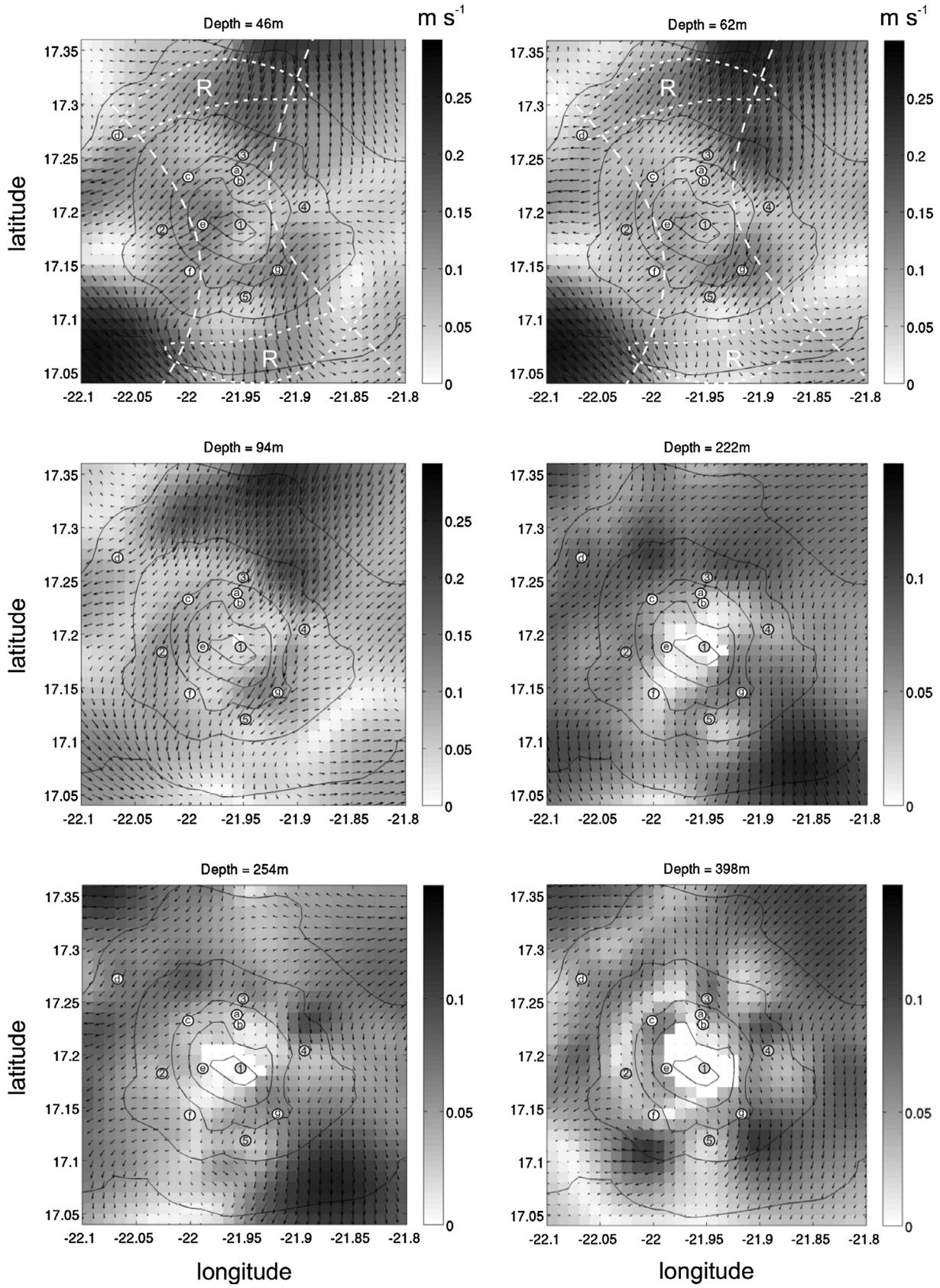

Fig. 3. Composite picture of ADCP-derived currents at different water levels at Senghor Seamount. The data set has not been de-tided. Isobaths: 200 m (centre), 500 m, 1000 m, 2000 m and 3000 m. Sampling stations as in Fig. 1b. Upper two plots: white dashed lines delineate the approximate regions of increased tidally-driven kinetic-energy dissipation (and turbulent-diffusive mixing); areas ('R') surrounded by dotted white lines: approximate regions where the initially upgoing seamount-generated semidiurnal internal-tide beams are thought to reflect from the sea surface (see black lines in Fig. 4b for beam paths).

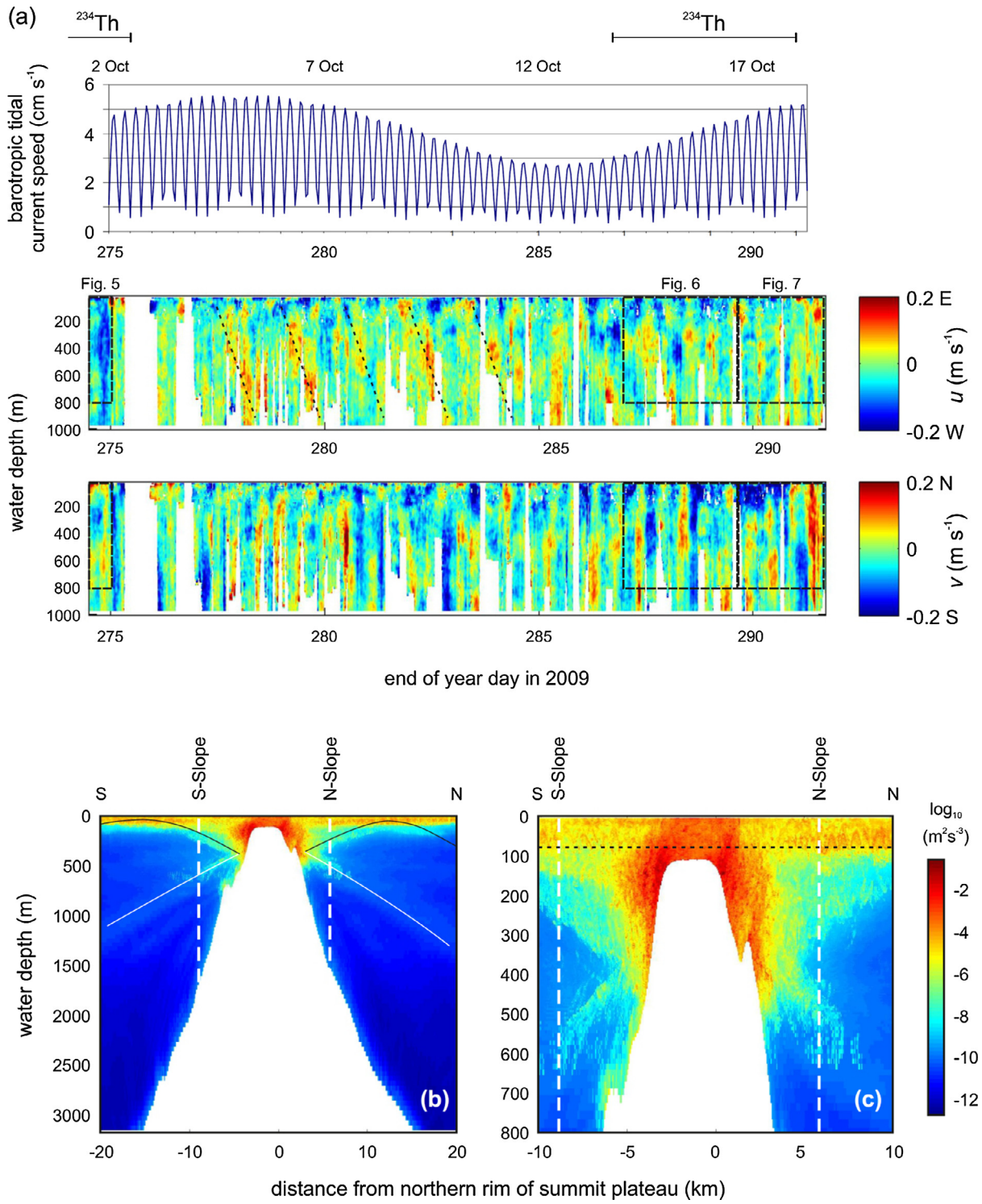

Fig. 4. (a) Top: barotropic tidal current speed near S-Ref as derived from the TPXO model (Egbert and Erofeeva, 2002); horizontal bars labelled '^{234}Th': time intervals during which the vast majority of ^{234}Th samples was collected. Centre: VM-ADCP-derived E-W current-speed component (eastward: positive values) for the ship time at Senghor Seamount in 2009; dotted lines: identical phases of near-inertial oscillations. Bottom: corresponding VM-ADCP-derived N-S current-speed component (northward: positive values). Dashed boxes: time intervals for which detailed ADCP time series are shown in Figs. 5–7. (b, c) N-S transect of numerically modelled kinetic-energy dissipation resulting from interactions of semidiurnal barotropic tidal flow over Senghor Seamount. (b) Whole seamount; (c) topmost 800 m of the seamount. The results are time-averaged over 3.5 tidal cycles and for a 2D model set-up. Vertical dashed lines: approximate locations of the sampling stations on the northern and southern mid slopes (N-Slope and S-Slope). Horizontal black dashed line in (c): lower boundary of the 'export layer' at the seamount. Black (white) solid lines in (b): paths of the initially upward (downward) beams of the semidiurnal internal tide that is generated on the uppermost northern and southern slopes of the seamount. The geometry of the internal-tide beams in the wider study area is shown in Fig. S3 of the Online Supplement.

(Fig. 4b and c), and with increased maximum current speeds compared to the 'shadow zones' of the water column (Fig. S3).

VM-ADCP time series at N-Ref and during transit between N-Ref and the seamount show spatiotemporal current-speed and

current-direction changes that are consistent with a beam emanating from Senghor Seamount and reflecting from the sea surface near N-Ref (Figs. 2a and b, S3); this was observed in October 2009 during cruise M79/3 of RV Meteor (Fig. 5a, c, e, g, i) and also in February 2013 during cruise 446 of RV Poseidon (Fig. 5b, d, f, h, j).

The MITgcm run also predicts that, in addition to beam formation, tidally oscillating flow that is forced over the summit plateau generates soliton-like internal waves that propagate horizontally in the topmost ~100 m and north- and southwards away from the seamount. This leads to increased maximum horizontal and vertical flow velocities (Fig. S3) and increased rates of kinetic

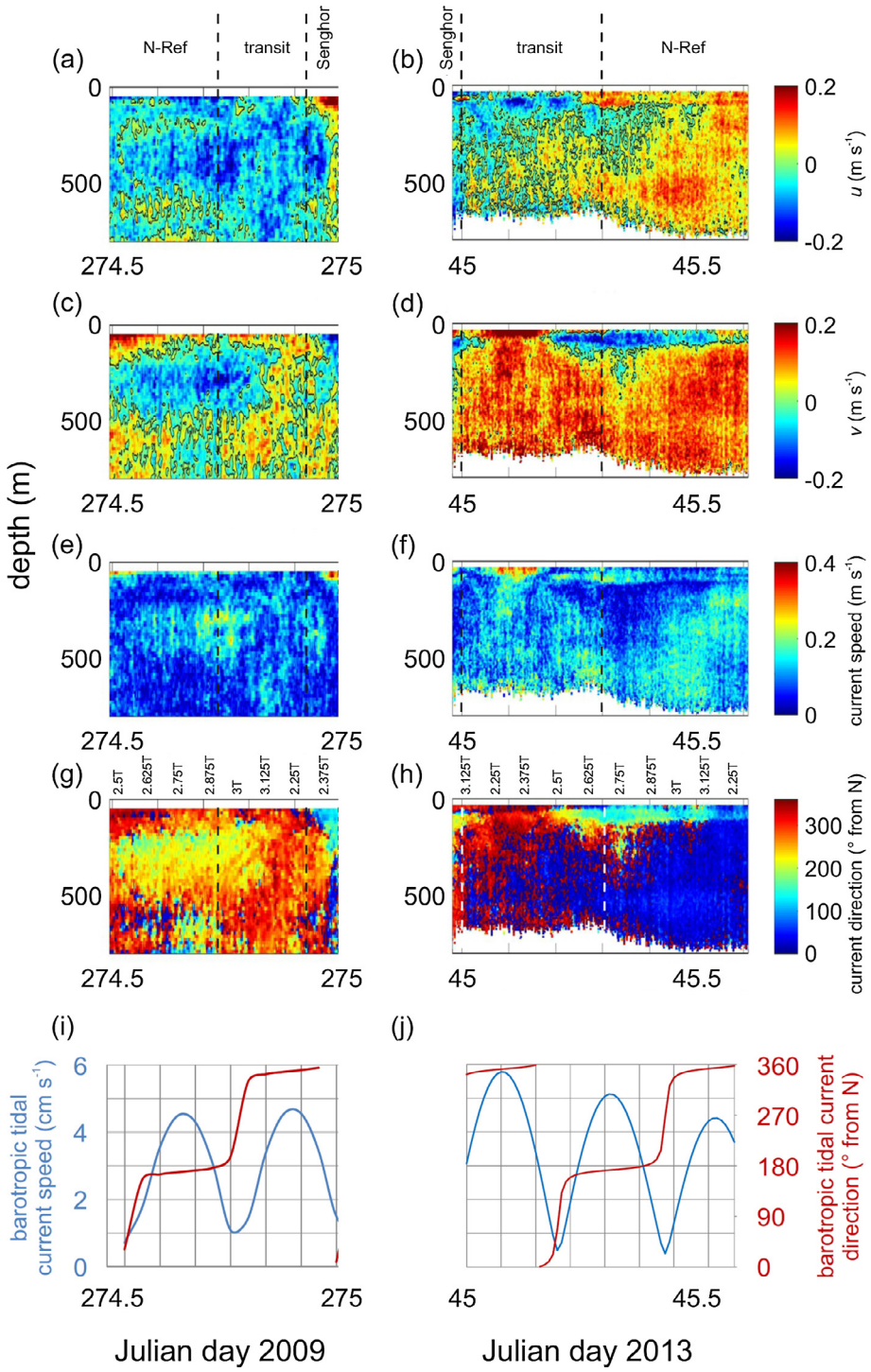

Fig. 5. VM-ADCP time series between Senghor Seamount and N-Ref. Left column: cruise M79/3 of RV Meteor in October 2009; right column: cruise 446 of RV Poseidon in February 2013. (a, b) E-W component, *u*, of the horizontal current velocity (positive values: eastward). (c, d) N-S component, *v*, of the horizontal current velocity (positive values: northward). (e, f) Magnitude of the horizontal current velocity that results from *u* and *v*. (g, h) Direction of the resulting current in degrees clockwise from N (N: 360° = 0°). (i, j) Current speed and direction of the barotropic tide (derived from the TPXO model of Egbert and Erofeeva (2002)). Numbers above (g) and (h) relate to points in time (tidal phases) of the MITgcm-derived internal tides in Fig. S3.

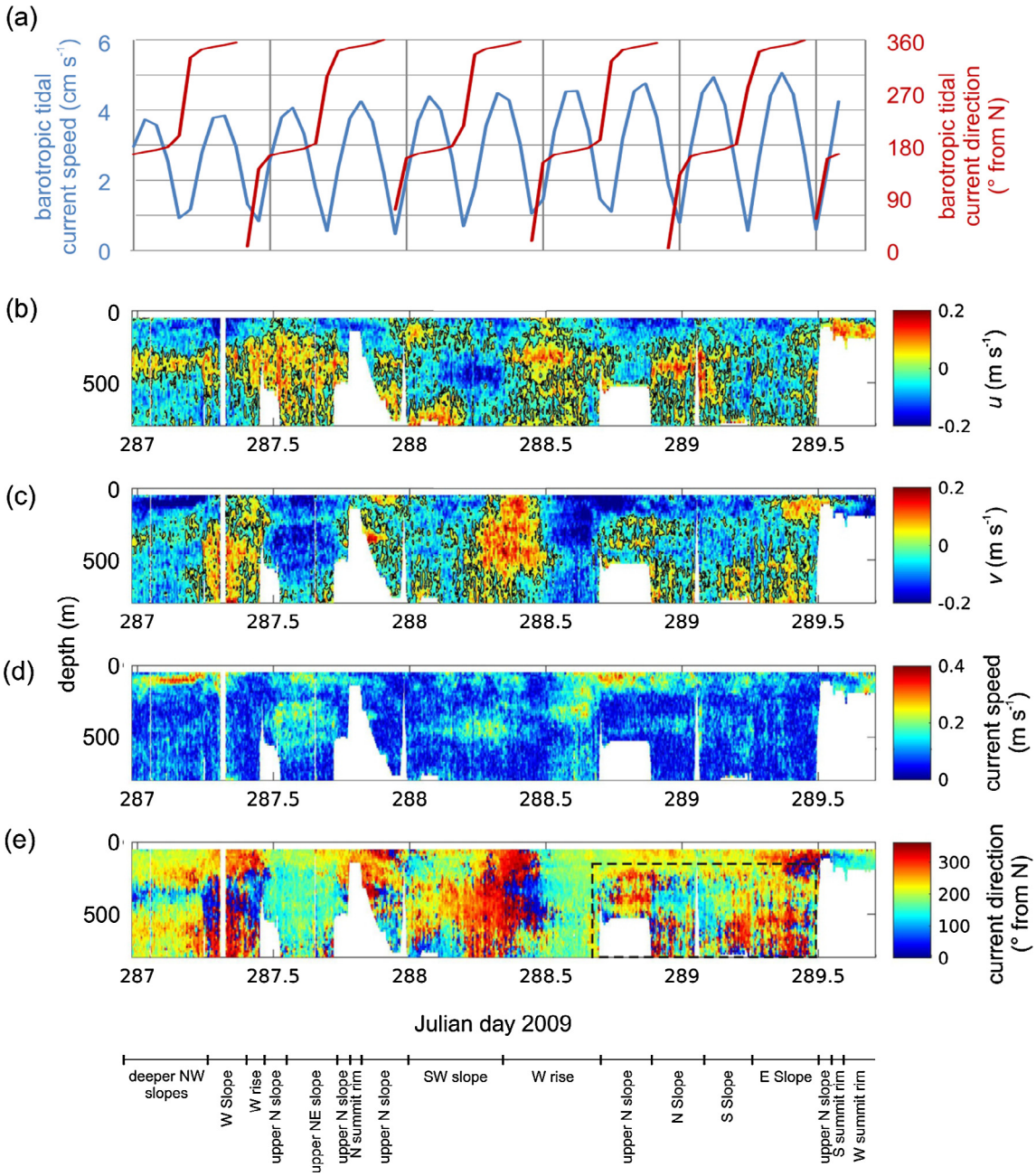

Fig. 6. Representative VM-ADCP time series at Senghor Seamount. The approximate locations of the ship are indicated at the bottom of the plot. (a) Current speed and direction of the barotropic tide (derived from the TPXO model of Egbert and Erofeeva (2002)). (b) E-W component, *u*, of the horizontal current velocity. (c) N-S component, *v*, of the horizontal current velocity. (d) Magnitude of the horizontal current velocity that results from *u* and *v*. (e) Direction of the resulting current in degrees clockwise from N (N: 360° = 0°). Note the emergence of the layered internal-wave structure in current directions after day 288.7 (dashed-line box) when peak barotropic tidal current speeds peak at >4.5 cm s^{-1} during their semidiurnal cycles.

energy dissipation (Fig. 4) around the summit plateau. Real-world evidence for these waves was also found in the VM-ADCP data: internal waves occurred in the topmost ~100 m, have a period of ~0.5 h and appear to propagate predominantly horizontally (they can be seen in Fig. 7, but are more noticeable in the example given in Fig. 8 as the vertical spatial resolution is twice as high and only the topmost 24 m of the ADCP record are blanked out).

The VM-ADCP results also revealed that, below the topmost ~150–200 m, there can be another type of higher-frequency internal wave that phase-propagates vertically (mostly upwards) and has vertical wave lengths of ~100 m and periods that often tend to be shorter than the one of semidiurnal oscillations and certainly shorter than the one of near-inertial oscillations (~40 h). These waves were observed during both October 2009 (Figs. 6 and 7) and February 2013 (Fig. 8). (They are particularly noticeable in the current directions between day 288.7 and 290.7 in Figs. 6e and 7e, also in current speed up to day 290.7 in Fig. 7d, and in *u*, *v*, current speed and current direction in Fig. 8). The fact that these waves were observed in October 2009 *and* in February 2013 is relevant as Senghor Seamount was located differently relative to nearby mesoscale eddies: in October 2009, Senghor was in the easternmost part of an elongated weak anticlockwise eddy (Fig. 2b), whereas in February 2013, Senghor was in the NW quarter of a strong circular westward-moving anticlockwise eddy (not

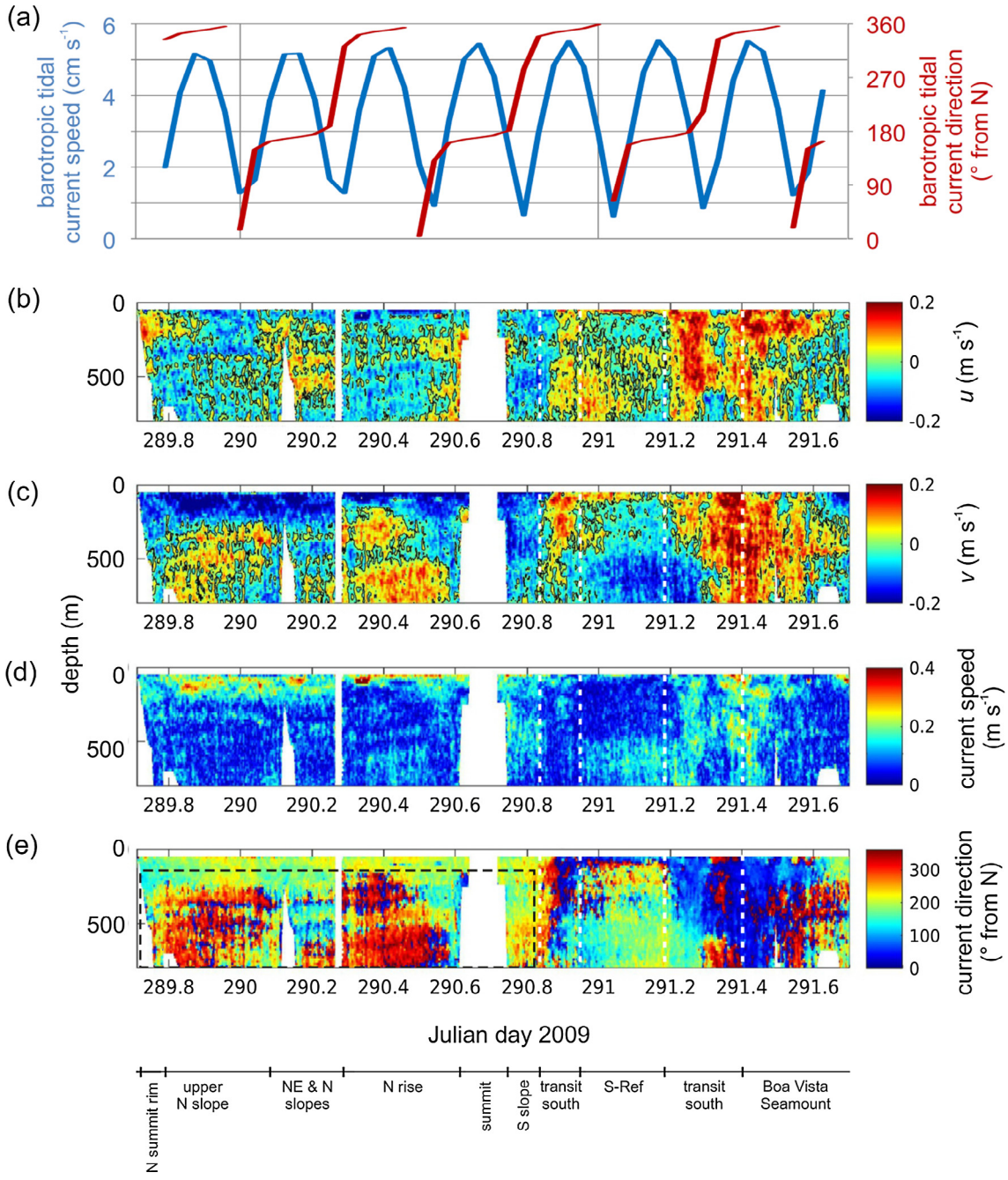

Fig. 7. Same as Fig. 6, but for the time interval of the transition from Senghor Seamount to S-Ref and further south to the Boa Vista Seamount. Note the layered internal-wave structure in current directions (dashed-line box) and speeds while barotropic tidal current speeds peak at >4.5 cm s^{-1} during their semidiurnal cycles. Also note that these internal waves became less obvious after the ship had left the seamount on day 290.85 while barotropic tidal current speeds still peaked at >4.5 cm s^{-1} during their semidiurnal cycles.

shown). Therefore, the location of Senghor Seamount relative to the mesoscale eddies seems to be unlikely to play an important role for these vertically phase-propagating higher-frequency internal waves.

The prevailing upward phase propagation indicates downward energy propagation and an energy source higher up in the water column. These waves became particularly prominent near/during spring tides when peak semidiurnal barotropic current speeds were $\geqslant$4.5 cm s^{-1} (see Fig. 6e: after day 288.7, when peak barotropic speeds start exceeding 4.5 cm s^{-1} (Fig. 6a), the waves become more obvious and can be seen up to day 290.7 in Fig. 7; the waves are also a constant feature in February 2013 when peak barotropic tidal current speeds were continuously >4.5 cm s^{-1}). The findings that the waves were most prominent in waters above the seamount slopes (Figs. 6–8), may reach northwards to at least the waters above the seamount rise (Fig. 7), did not occur at N-Ref (Fig. 5) and only occurred very faintly at S-Ref (Fig. 7), further support the notion that the waves were generated at Senghor Seamount.

Overall, the evidence suggests that these higher-frequency internal waves were tidally generated at the seamount. Given the short wave periods and short vertical wave lengths, these waves might be (related to) higher harmonics of the internal-tide beams that emanate from the uppermost parts of Senghor Seamount (this

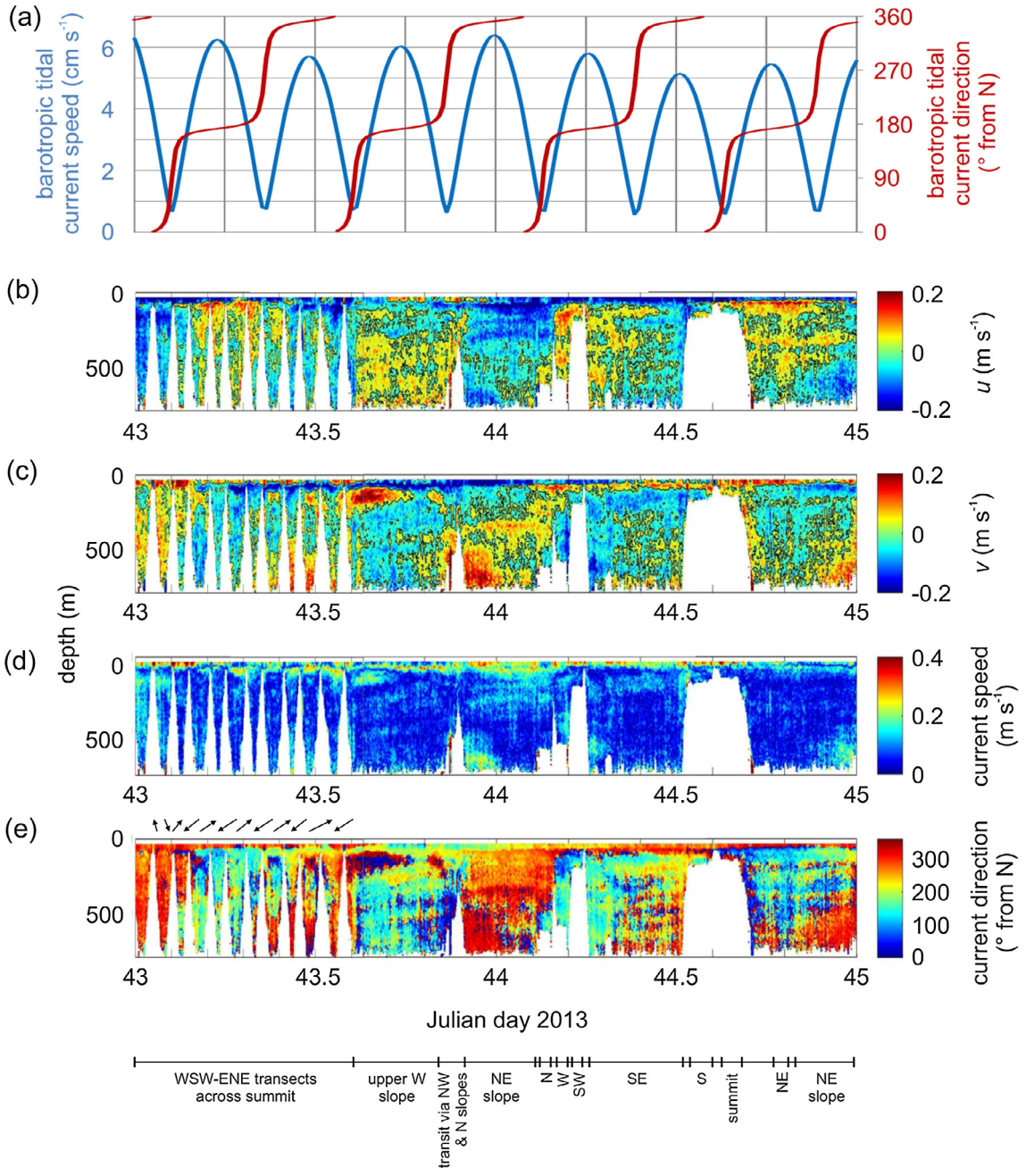

Fig. 8. Same as Fig. 6, but for a representative VM-ADCP time series at Senghor Seamount during cruise 446 of RV Poseidon in February 2013. Arrows above plot (d) indicate directions of the ship's movements during a NNW excursion from the summit (first two arrows) and the repeat WSW-ENE transects across the summit (all other arrows). Note the prominent layered internal-wave structure in current directions and speeds throughout the time series when barotropic tidal current speeds peak at >4.5 cm s^{-1} during their semidiurnal cycles.

is especially likely to be the case for largely supercritical seamounts such as Senghor Seamount; Lamb, 2004). Because of the short wave lengths these waves may dissipate relatively quickly, contributing to increased rates of energy dissipation near the upper seamount, especially when they interact with the high mass-density stratification in the pycnocline.

Finally, there is also hydrographic evidence for the importance of tidally generated higher-frequency internal waves at this seamount. Instantaneous mixed-layer thicknesses ranged from only ~5 m up to ~20 m (Figs. 10 and 11). Underneath the mixed layer was an abrupt pycnocline where the main part of the pycnocline was only ~5–20 m thick. At stations where several mass-density profiles could be obtained (e.g., N-Ref: Fig. S4) mixed-layer and pycnocline thicknesses varied temporally on time scales as short as hours to days. And at greater depths of 100 s of meters, there were fairly abrupt vertical shifts (by 10 s of meters) of isohalines, isotherms and oxygen isopleths across the seamount (Fig. 9). Due to the paucity of the hydrographic dataset it is impossible to tell whether this is temporal or spatial variability or both. In any case, the existence of these abrupt shifts and the evidence for temporally highly variable mixed-layer and pycnocline thicknesses suggest that fluid dynamics around the upper seamount can be vigorous, probably due to the higher-frequency seamount-generated internal waves.

In summary, there are several lines of evidence indicating that tides play a prominent role in controlling fluid dynamics at

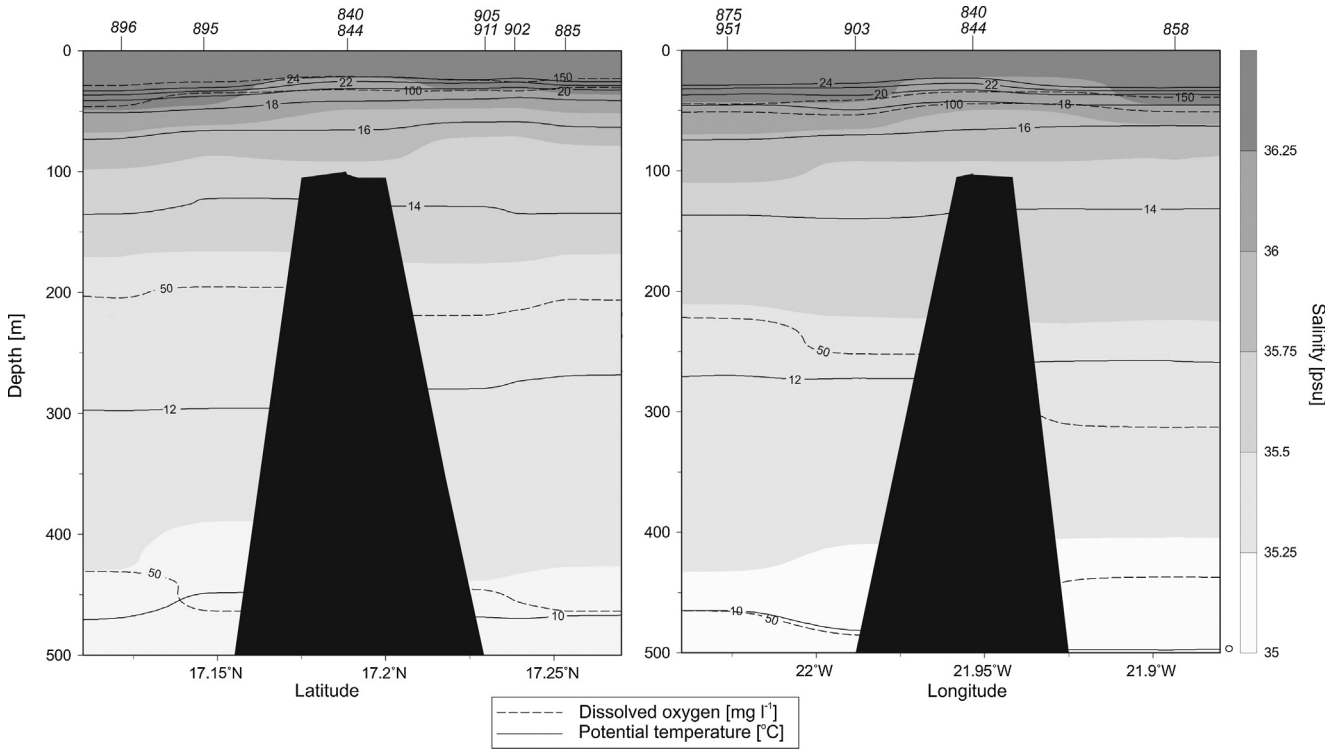

Fig. 9. Composite N-S (left) and E-W (right) hydrographic sections across the summit of Senghor Seamount. Each plot displays salinity (shaded background), potential temperature (solid lines: °C) and dissolved oxygen (dashed lines: mg O_2 L^{-1}). CTD station numbers used to produce these plots are displayed above their cast locations in each plot. Created in ODV with VG-gridding interpolation (Schlitzer, 2002). The bathymetry was constructed by interpolating between station bottom depths, which were determined via a swath multibeam survey carried out during the cruise (Fig. 1b).

Senghor Seamount. This could have implications for nutrient redistribution and particle dynamics in the topmost few 100 s of meters of the water column around the seamount, potentially influencing POC export.

3.1.4. Physical oceanography: summary and conclusion

The available physical-oceanographic information leads to the following conclusions regarding the flow dynamics around Senghor Seamount at the time of the study (Objective O1). (1) Larger-scale regional features such as the CVFZ and the Mauritanian upwelling system did not play a role for this study. (2) S-Ref can be used as a reference site for the seamount stations. (3) Within the topmost ~200 m of the water column, low-frequency background flow impinged on the seamount from the northeast, contributing to isopycnal doming over the summit. (4) At depths greater than ~200 m and down to at least ~600 m, there is evidence for clockwise recirculation of near-seafloor waters around the seamount (a deep Taylor column and/or weak tidal rectification); there is no evidence for seamount-trapping of near-seafloor waters down to ~200–250 m. (5) Higher-frequency fluid dynamics were primarily influenced by barotropic tidal forcing, leading to the generation of internal-tide beams and soliton-like internal waves that preferentially propagate away to the north and south and are thought to form a N-S 'screen' of intensified kinetic energy dissipation (and probably intensified vertical mixing) that runs across the upper seamount. (6) In the topmost hundreds of meters of the water column, another type of internal wave was observed over the seamount slopes and also further towards the north and south away from the seamount. These waves are also likely to be seamount-generated, could be higher harmonics of the main internal tide, and probably also contribute to the screen of increased rates of energy dissipation that runs across the upper seamount. (7) As the dissipation screen was orientated approximately orthogonally to the low-frequency background inflow from the NE, the waters of the background flow were passing *through* this screen at the time of this study.

The main physical-oceanographic result is that tides seem to play a key role in controlling the fluid dynamics at Senghor Seamount and result in a screen of enhanced kinetic energy dissipation that runs across the seamount in the NNW-SSE direction and was traversed by the background flow at the time of this study. The distribution of dissipation of kinetic energy is likely to be of importance for seamount biogeochemistry as it may influence vertical mixing (Waterhouse et al., 2014) (and therefore nutrient redistribution) and potentially also particle aggregation and/or disaggregation (and therefore vertical flux of particulate matter) (Burd and Jackson, 2009).

3.2. Thorium-234

3.2.1. Distribution of total and particulate ^{234}Th

Total ^{234}Th activities (A^t_{Th}) in the topmost 250 m of the water column ranged from 1.46 up to 2.62 dpm L^{-1} (Table 2). At all sites there were significant $^{234}Th/^{238}U$ disequilibria ($A^t_{Th} < A_U$), almost always located within the topmost 75 m, i.e., reaching well below the surface mixed layer (Figs. 10 and 11). There was no evidence for ^{234}Th excess ($A^t_{Th} > A_U$) which is sometimes observed right below the surface layer and interpreted in terms of rapid particulate-matter breakdown.

Particulate ^{234}Th activities (A^p_{Th}) of the >53 µm samples (Table 3) were always higher at 50 m depth (32 m depth at N-Ref) compared to 150 m depth (90 m at the Summit). The highest value at 50 m was found above the summit plateau (0.071 ± 0.018 dpm L^{-1}) and the second highest at N-Slope (0.036 ± 0.002 dpm L^{-1}); the lowest occurred at S-Ref (0.015 ± 0.000 dpm L^{-1}). The highest value at 150 m depth was found at N-Slope (0.032 ± 0.005 dpm L^{-1})

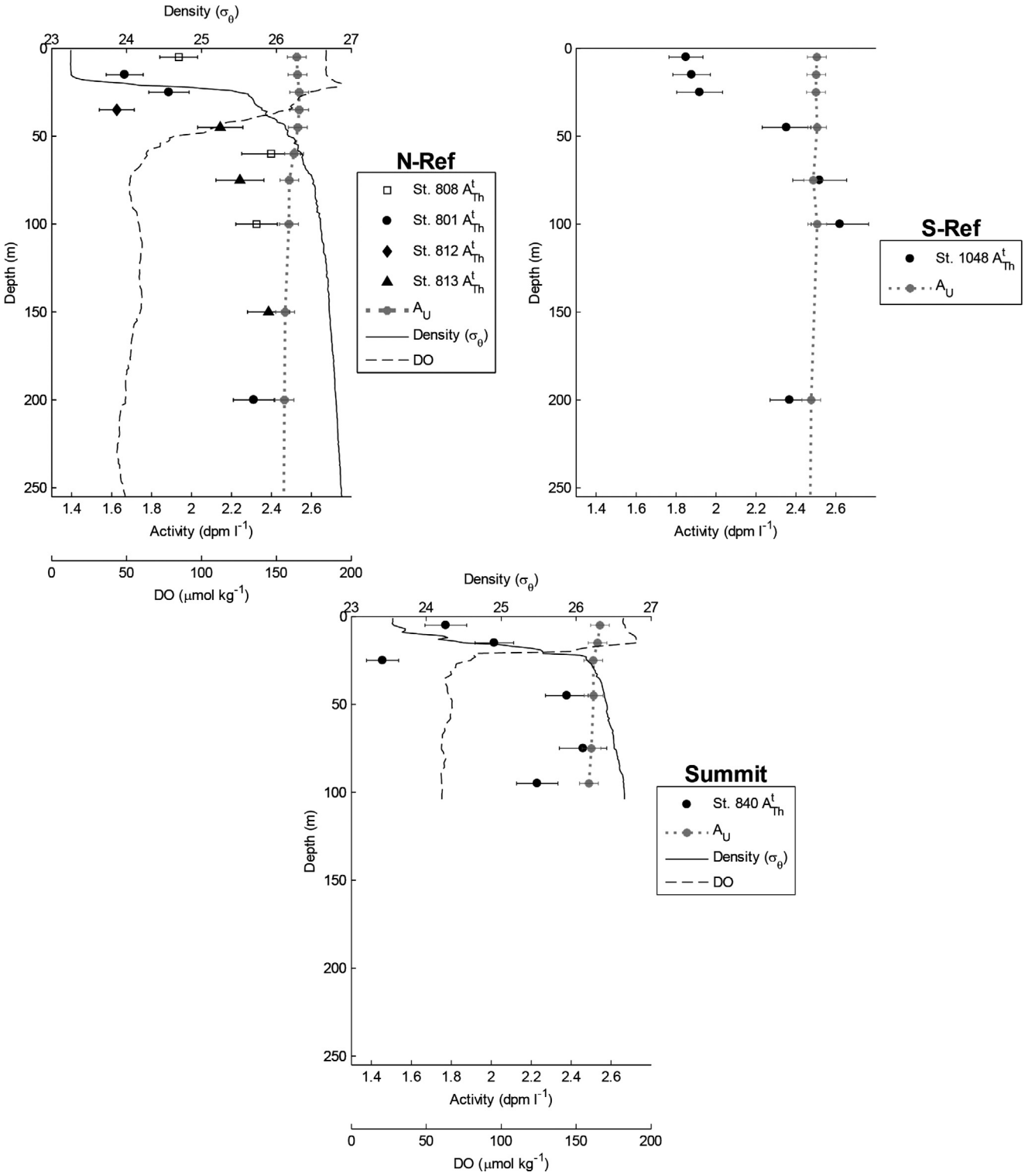

Fig. 10. Profiles of total ^{234}Th activity (A^t_{Th}), ^{238}U activity (A_U), mass density of water (σ_θ; solid line) and dissolved oxygen (dashed line) at the N-Ref (top-left), S-Ref (top-right) and Summit (bottom). σ_θ and dissolved-oxygen data have not been included in the S-Ref profile due to an equipment malfunction. Error bars for the A^t_{Th} and A_U data are one standard deviation.

and the lowest at W-Slope (0.009 ± 0.000 dpm L^{-1}). The general range of values is very similar to the range of values found by Owens et al. (2015) in this study area at the end of October 2010.

Activities of the 0.7–53 µm samples in the topmost 150 m (Table 3) were found to be 0.044 ± 0.016 dpm L^{-1} up to 0.227 ± 0.023 dpm L^{-1} (average: 0.144 dpm L^{-1}). The higher activity values of this study are very similar to values reported by Owens et al. (2015) for the surface waters of the same region in late October 2010. The values from the Summit, however, look low (about 1/2 to 1/4) in comparison to the results of Owens et al. (2015). Unfortunately, our ^{234}Th data set for 0.7–53 µm particles is incomplete as not all relevant depths and locations could be sampled.

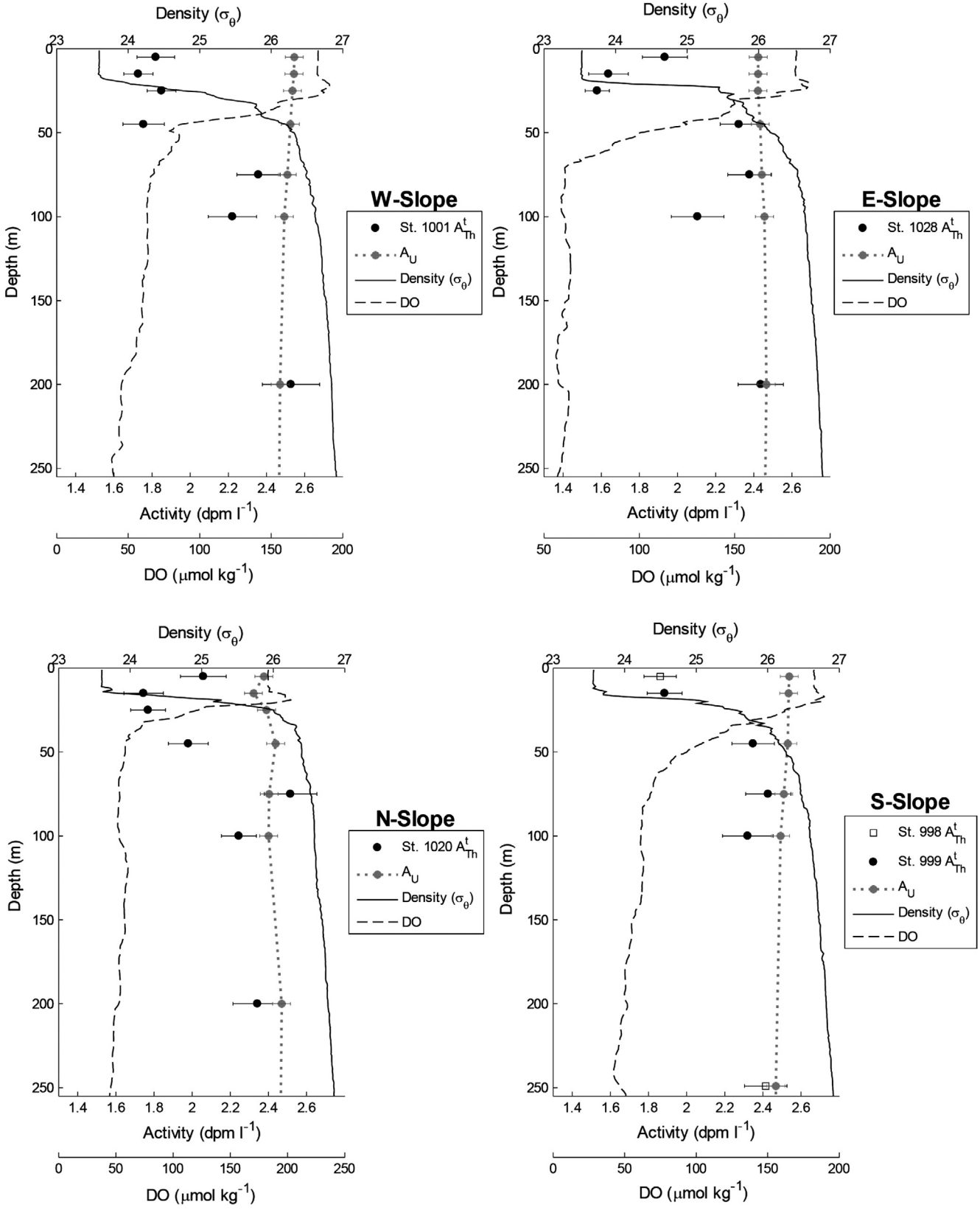

Fig. 11. Same as Fig. 10, but for the W-Slope (top-left), E-Slope (top-right), N-Slope (bottom-left) and S-Slope (bottom-right).

3.2.2. Thorium-234 export fluxes

As outlined by Owens et al. (2015), in previous studies different approaches have been used to define the water layer for which export fluxes are calculated (the 'export layer'). There seem to be three main procedures: (1) The export layer is defined through the depth at which $^{234}Th/^{238}U$ equilibrium is reached. This

Table 2
Radioactivities of ^{238}U (A_U) and total ^{234}Th (A^t_{Th}), expressed as disintegrations per minute per litre of seawater (dpm L^{-1}). Uncertainties are given as one propagated standard deviation (1SD).

Station	Site	Sample depth (m)	A_U (dpm L^{-1})[a]	A_U: 1SD (dpm L^{-1})[a]	A^t_{Th} (dpm L^{-1})	A^t_{Th}: 1SD (dpm L^{-1})
808	*N-Ref*	5	2.527	0.047	1.94	0.09
801	*N-Ref*	15	2.530	0.047	1.67	0.09
801	*N-Ref*	25	2.539	0.047	1.89	0.10
812	*N-Ref*	35	2.539	0.047	1.63	0.09
813	*N-Ref*	45	2.532	0.047	2.14	0.11
808	*N-Ref*	60	2.513	0.047	2.40	0.15
813	*N-Ref*	75	2.490	0.047	2.24	0.12
808	*N-Ref*	100	2.488	0.047	2.33	0.10
813	*N-Ref*	150	2.468	0.047	2.39	0.11
801	*N-Ref*	200	2.465	0.047	2.31	0.10
812	*N-Ref*	1396	2.436	0.047	2.45	0.13
812	*N-Ref*	1398	2.436	0.047	2.43	0.13
812	*N-Ref*	1400	2.436	0.047	2.24	0.10
812	*N-Ref*	1402	2.436	0.047	2.30	0.16
812	*N-Ref*	1404	2.436	0.047	2.44	0.22
1020	*N-Slope*	5	2.376	0.047	2.06	0.12
1020	*N-Slope*	15	2.322	0.047	1.75	0.10
1020	*N-Slope*	25	2.390	0.047	1.77	0.09
1020	*N-Slope*	45	2.438	0.047	1.98	0.10
1020	*N-Slope*	75	2.404	0.047	2.52	0.14
1020	*N-Slope*	100	2.401	0.047	2.24	0.09
1020	*N-Slope*	200	2.469	0.047	2.34	0.13
840	*Summit*	5	2.544	0.047	1.77	0.10
840	*Summit*	15	2.532	0.047	2.02	0.10
840	*Summit*	25	2.511	0.047	1.46	0.08
840	*Summit*	45	2.513	0.047	2.38	0.11
840	*Summit*	75	2.502	0.047	2.46	0.12
840	*Summit*	95	2.489	0.047	2.23	0.10
1001	*W-Slope*	5	2.546	0.047	1.82	0.10
1001	*W-Slope*	15	2.544	0.047	1.73	0.08
1001	*W-Slope*	25	2.536	0.047	1.85	0.08
1001	*W-Slope*	45	2.525	0.047	1.76	0.11
1001	*W-Slope*	75	2.509	0.047	2.36	0.11
1001	*W-Slope*	100	2.493	0.047	2.22	0.13
1001	*W-Slope*	200	2.472	0.047	2.53	0.15
1028	*E-Slope*	5	2.423	0.047	1.93	0.12
1028	*E-Slope*	15	2.423	0.047	1.64	0.10
1028	*E-Slope*	25	2.422	0.047	1.58	0.06
1028	*E-Slope*	45	2.434	0.047	2.32	0.10
1028	*E-Slope*	75	2.442	0.047	2.38	0.12
1028	*E-Slope*	100	2.456	0.047	2.11	0.14
1028	*E-Slope*	200	2.466	0.047	2.44	0.12
998	*S-Slope*	5	2.538	0.047	1.86	0.08
999	*S-Slope*	15	2.535	0.047	1.88	0.09
999	*S-Slope*	45	2.531	0.047	2.35	0.11
999	*S-Slope*	75	2.509	0.047	2.43	0.12
999	*S-Slope*	100	2.492	0.047	2.32	0.13
998	*S-Slope*	249	2.468	0.047	2.41	0.11
1048	*S-Ref*	5	2.505	0.047	1.85	0.08
1048	*S-Ref*	15	2.502	0.047	1.88	0.09
1048	*S-Ref*	25	2.500	0.047	1.92	0.11
1048	*S-Ref*	45	2.506	0.047	2.35	0.12
1048	*S-Ref*	75	2.487	0.047	2.52	0.13
1048	*S-Ref*	100	2.507	0.047	2.62	0.14
1048	*S-Ref*	200	2.477	0.047	2.37	0.10

[a] Calculated from the relationship between ^{238}U and salinity given by Owens et al. (2011).

approach typically takes into account the combined effect of both near-surface disequilibria where $A^t_{Th} < A_U$ and excess layers where $A^t_{Th} > A_U$ (if present). (2) In some cases disequilibria reach into waters that are deeper than the photosynthetically active surface waters. The export layer is then defined based on the layer of water in which active photosynthesis is thought to take place. This approach in itself has taken different forms and was based on, for instance, the 1%-depth-level of photosynthetically active radiation (PAR), the 10%-depth-level of maximum chlorophyll fluorescence, or estimates of the 'compensation depth' where gross photosynthetic organic-carbon production and organic-carbon respiration cancel each other out and NPP is zero. (3) In some cases a comparatively arbitrary depth was chosen as the lower boundary of the export layer. A number of studies have used the 100 m cut-off.

Owens et al. (2015) showed for our study region that water layers with disequilibria $A^t_{Th} < A_U$ coincided very well with the distribution of photosynthetically active organisms. We, therefore, chose the first of the above approaches (the equilibrium-depth approach) to calculate ^{234}Th export for this study. However, to

Table 3
Radioactivities of ^{234}Th in SAPS-collected particulate matter (A^p_{Th}), expressed in terms of dpm per litre of filtered seawater. Uncertainties are given as one propagated standard deviation (1SD). Mesh: nominal pore size of 53 μm; GF/F: nominal pore size of 0.7 μm, i.e., the data correspond to particles in the nominal size fraction 0.7–53 μm. GF/F data are corrected for ^{234}Th sorption (see Section 2.2.2.2 for details).

Station	Site	Filter type	Depth (m)	A^p_{Th} (dpm L^{-1})	A^p_{Th}: 1SD (dpm L^{-1})
808	*N-Ref*	mesh	32	0.023	0.001
808	*N-Ref*	GF/F	32	0.206	0.059
803	*N-Ref*	mesh	150	0.013	0.001
803	*N-Ref*	GF/F	150	0.161	0.017
1039	*N-Slope*	mesh	50	0.036	0.002
885	*N-Slope*	mesh	150	0.032	0.005
840	*Summit*	mesh	50	0.071	0.002
840	*Summit*	GF/F	50	0.044	0.016
840	*Summit*	mesh	90	0.019	0.002
840	*Summit*	GF/F	90	0.106	0.007
1002	*W-Slope*	mesh	50	0.024	0.001
875	*W-Slope*	mesh	150	0.009	0.000
875	*W-Slope*	GF/F	150	0.123	0.012
1029	*E-Slope*	mesh	50	0.023	0.001
858	*E-Slope*	mesh	150	0.015	0.001
858	*E-Slope*	GF/F	150	0.227	0.023
999	*S-Slope*	mesh	50	0.021	0.001
896	*S-Slope*	mesh	150	0.012	0.001
1048	*S-Ref*	mesh	50	0.015	0.001
1048	*S-Ref*	mesh	150	0.014	0.001

facilitate direct comparison with studies that used the '100 m-cut-off' approach, additional export-flux calculations were carried out using 100 m as the lower boundary of the export layer.

In order to estimate the net ^{234}Th-flux (P) from the disequilibrium layer, a single-box steady-state model (Coale and Bruland, 1987; Savoye et al., 2006) was applied according to

$$P = \lambda \int_0^z (A_U - A^t_{Th}) dz \quad (1)$$

where λ is the decay constant of ^{234}Th ($\lambda = \ln 2/t_{1/2} \approx 0.02876$ d^{-1}) and z is the depth at which ^{234}Th/^{238}U equilibrium is met. An implicit assumption of Eq. (1) is that there is no net physical-oceanographic transport of ^{234}Th into or out of a sampling site due to turbulent diffusion and/or advection that is superimposed on spatial A^t_{Th} gradients.

At most stations equilibrium was reached at 75 m; only at N-Ref it was reached already at 60 m. Because of the shallow water above the summit plateau and the possible influence of resuspension on ^{234}Th dynamics in the water column it is not possible to unequivocally identify the export layer for the Summit station. However, an equilibrium value was detected at 75 m depth at the Summit site and z = 75 m was therefore used to estimate a notional export value for this location. The robustness of this estimate will be discussed in more detail in Section 3.4.2 below.

^{234}Th export fluxes that were derived through the equilibrium-depth approach ranged from 616 ± 61 up to 1306 ± 90 dpm m^{-2} d^{-1}, with errors given as 1 propagated standard deviation (1SD) (Fig. 12a; Table 4). In the far field, a greater flux was found for N-Ref compared to S-Ref. Significant differences were observed between some of the seamount sites: most notably, the W-Slope site displayed the highest flux of all the slope sites (1306 ± 90 dpm m^{-2} d^{-1}) at approximately twice the estimated magnitude of flux observed at the S-Slope (712 ± 104 dpm m^{-2} d^{-1}) and even being slightly higher than at N-Ref (990 ± 61 dpm m^{-2} d^{-1}). Flux estimates that were derived by the '100 m-cut-off' approach were indistinguishable from, or only slightly higher than, the results of the equilibrium-depth approach (Fig. 12a; Table 4).

Before the ^{234}Th flux results can be used to calculate POC export, two key assumptions of Eq. (1) need to be scrutinised: the steady-state assumption and the assumption of negligible net physical-oceanographic transport of ^{234}Th. This is done in detail in the Online Supplement S5. In summary, the seamount sites N-Slope, S-Slope, Summit and W-Slope are likely to be associated with underestimates of ^{234}Th export fluxes. The highest underestimate probably occurred for W-Slope as there is a combination of the effects of net advective input and sustained vertical mixing. The extent of the underestimate at Summit is uncertain because of the possible added influence of resuspended sediments on ^{234}Th dynamics (see the more detailed discussion in Section 3.4.2). Overall, however, it seems safe to conclude that all seamount sites have higher ^{234}Th export fluxes than S-Ref; and there is strong evidence for increasing export in the downstream direction across the seamount. For completeness, it also needs to be stressed that, because of the low zooplankton (<20 mm) biomass at Senghor Seamount (<0.1–0.2 g m^{-3} in the topmost ~100 m of the water column: Denda and Christiansen, 2014; Denda et al., 2016), zooplankton-associated vertical transport of ^{234}Th is most certainly negligible in this area (Rodriguez y Baena et al., 2006).

3.3. Particulate organic carbon (POC) and particulate nitrogen (PN)

In the >53 μm size fraction, POC and PN concentrations were often higher at 50 m (32 m at N-Ref) than at 150 m (90 m at the Summit) (Table 5). Particles >53 μm are thought to constitute the bulk of the settling flux into the deep interior ocean and the decreasing concentrations with increasing depth support the view of active export of particulate matter. In the far field there is an approximate halving of POC and PN concentrations in the >53 μm size fraction if one compares N-Ref to S-Ref. The seamount is also associated with significant variability. At 50 m POC concentrations at the seamount were ~2–5 times higher than at S-Ref, suggesting a seamount effect on the formation of larger particles. POC concentrations at the seamount at 150 m were up to ~4 times higher than at S-Ref, also suggesting a seamount effect; however, the effect is reduced compared to 50 m. Interestingly, the POC concentration at W-Slope at 150 m is very low and similar to the low POC concentration at S-Ref at 150 m. This low POC concentration at 150 m in combination with a still comparatively high POC concentration at 50 m and a high ^{234}Th export flux estimate suggests that

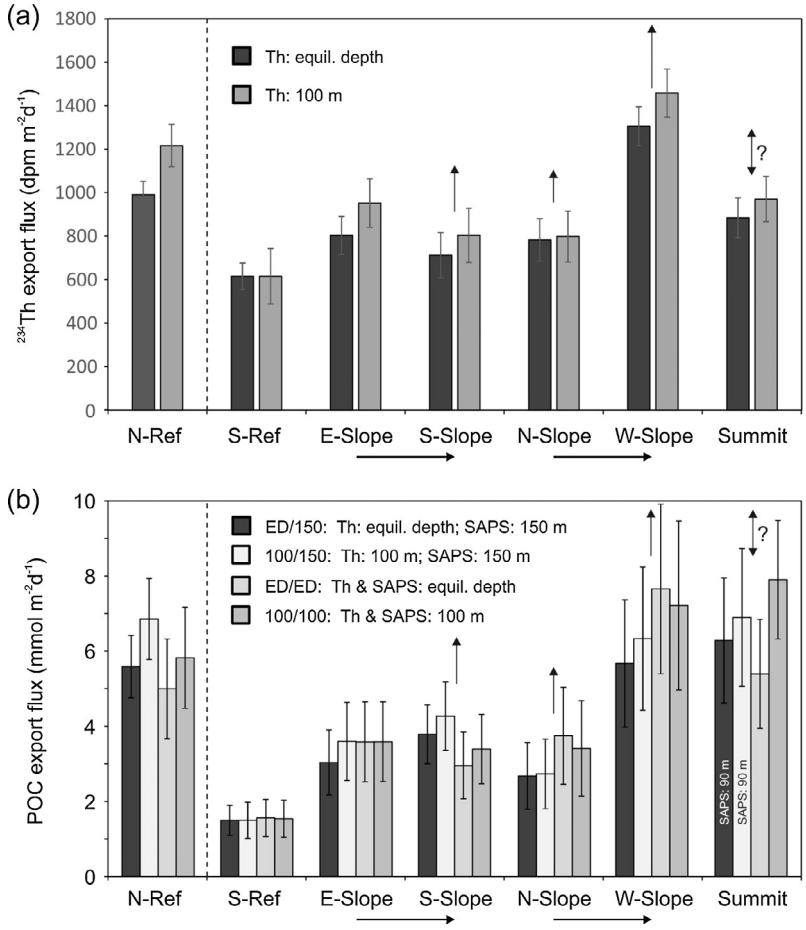

Fig. 12. (a) Export fluxes of ^{234}Th. Results for two different ways of calculating the fluxes are shown. (b) Export fluxes of POC. Results for four different ways of calculating the fluxes are shown. N-Ref is not viewed as a suitable reference site and separated from the other station results by the vertical dashed line. S-Ref was a suitable reference site for the seamount stations. Horizontal arrows below abscissa: E-Slope and N-Slope are viewed as sites that are located approximately upstream of S-Slope and W-Slope, respectively. Upward arrows indicate probable underestimates. Bidirectional arrow with '?': here, it is unclear whether there is an under- or overestimate. Error bars: ± one propagated standard deviation.

the waters sampled at W-Slope were strongly affected by recent or ongoing export of particulate matter. This view is also supported by the higher concentrations at 50 m and especially 150 m at the N-Slope station that is located upstream of W-Slope: as W-Slope is the downstream seamount station the results from this station can be interpreted in terms of a maturing seamount-derived export signal.

Broadly speaking, the horizontal concentration trends at 50 m are qualitatively similar for the 0.7–53 μm size fraction, but absolute concentrations were much higher (by about an order of magnitude) than in the >53 μm size fraction (Table 5). At 150 m POC concentrations in the 0.7–53 μm size fraction were generally low across the study region. However, at the seamount, significant POC concentration drops (by factors of ~2–7) occurred in the 0.7–53 μm size fraction if one moved from 50 m to 150 m; by contrast, the concentrations at 50 m and 150 m at S-Ref were very similar and low. This suggests formation of particulate material in the topmost 10 s of meters of the water column at the seamount. Finally, at 50 m, the molar C/N ratios (~10–11) for the organic matter in the 0.7–53 μm size fraction are higher more upstream (N-Slope and S-Ref) than at the other more downstream seamount stations (~6–8), possibly indicating that the formed particles contain comparatively fresh (N-rich) organic material. Overall, the POC- and PN-derived information points to formation of fresh particulate organic matter in the near-surface waters at the seamount.

3.4. POC export flux

Estimates of POC export fluxes can now be derived by multiplying the ^{234}Th-export flux, P (Eq. (1)), with the POC/A^{p}_{Th} ratio on the larger faster-settling particles (>53 μm). For the topmost few 100 s of meters of the oceanic water column, it has been shown that the POC/A^{p}_{Th} ratio on settling particles often decreases with depth, with much of the overall decline completed within the topmost 100 m of the water column and the steepest part of the drop occurring in the topmost tens of meters (Buesseler et al., 2006; Owens et al., 2015). The choice of depth from which to derive POC/A^{p}_{Th} ratios may, therefore, significantly influence the outcome of the POC export flux calculation and its uncertainty.

In this study we are interested in POC export *from* the export layer into the deep interior water column and not in vertical flux distribution *throughout* the export layer or export that only reaches the twilight zone. To arrive at such export estimates for all sites (except Summit which is too shallow), the POC/A^{p}_{Th} ratios determined for particles >53 μm at 150 m were used. Despite the high level of confidence in this original approach (ED/150: ^{234}Th flux at equilibrium depth (ED) and POC/A^{p}_{Th} ratio at 150 m depth), three additional approaches were applied to calculate estimates of POC export. This was done to facilitate comparison with other studies that used the '100 m cut-off' approach for ^{234}Th export calculations and to consider further potential sources of uncertainty. The first additional approach (100/150) used POC/A^{p}_{Th} values from 150 m

Table 4
Estimates of ^{234}Th export fluxes, POC/Th ratios in > 53 μm particles, and POC export fluxes. Uncertainties are given as one propagated standard deviation (1SD).

Site	Lower boundary depth of export layer[a] (m)	^{234}Th export (dpm m^{-2} d^{-1})	1SD	POC/^{234}Th[b] (μmol dpm^{-1})	1SD	POC export[e] (mmol m^{-2} d^{-1})	1SD
N-Ref	60	990	61	3.63[c]	1.32[c]	5.58	0.83
	100	1216	97	5.63	0.76	6.84	1.08
						4.99	1.33
						5.81	1.35
N-Slope	75	783	98	5.1	1.87	2.67	0.88
	100	799	117	3.42	1.05	2.73	0.93
						3.74	1.29
						3.40	1.27
Summit	75	884	92	2.96	1.01	6.27	1.66
	100	971	104	7.10[d]	1.73[d]	6.89	1.83
						5.38	1.45
						7.89	1.58
W-Slope	75	1306	90	5.55	1.73	5.66	1.70
	100	1458	111	4.34	1.26	6.32	1.90
						7.65	2.26
						7.20	2.25
E-Slope	75	803	87	3.75	1.05	3.03	0.86
	100	952	111	3.77	1.00	3.59	1.04
						3.58	1.06
						3.58	1.06
S-Slope	75	712	104	3.13	1.11	3.78	0.78
	100	803	125	5.31	0.77	4.26	0.91
						2.95	0.88
						3.39	0.92
S-Ref	75	616	61	2.56	0.63	1.49	0.40
	100	616	128	2.42	0.60	1.49	0.48
						1.56	0.50
						1.53	0.49

[a] Upper row: depth at which ^{234}Th/^{238}U equilibrium is reached; lower row: constant assumed lower boundary at 100 m depth.
[b] Upper row: 50 m depth; lower row: 150 m depth.
[c] At 32 m depth.
[d] At 90 m depth.
[e] Row 1 (approach ED/150): ^{234}Th flux based on equilibrium depth, POC/^{234}Th ratio from 150 m; row 2 (approach 100/150): ^{234}Th flux based on assumed 100 m depth boundary of export layer, POC/^{234}Th ratio from 150 m; row 3 (approach ED/ED): ^{234}Th flux based on equilibrium depth, POC/^{234}Th ratio linearly interpolated to the equilibrium depth between 50 m and 150 m; row 4 (approach 100/100): ^{234}Th flux based on assumed 100 m depth boundary of export layer, POC/^{234}Th ratio linearly interpolated to 100 m depth between 50 m and 150 m.

Table 5
Particulate organic carbon and particulate nitrogen concentrations (μg L^{-1}) and molar C/N ratios in the particulate organic matter associated with small (0.7–53 μm) and large (>53 μm) SAPS-collected particles. Uncertainties are given as one propagated standard deviation (1SD).

Station	Site	Depth (m)	0.7–53 μm						>53 μm					
			PN	PN 1SD	POC	POC 1SD	Molar C:N	C/N 1SD	PN	PN 1SD	POC	POC 1SD	Molar C:N	C/N 1SD
808	N-Ref	32	3.79	0.12	22.6	0.66	6.95	0.30	0.19	0.06	1.00	0.36	6.19	2.96
803	N-Ref	150	0.71	0.02	4.53	0.17	7.39	0.35	0.13	0.02	0.86	0.10	7.99	1.54
1039	N-Slope	50	6.14	0.14	30.17	2.43	5.74	0.48	0.44	0.18	2.21	0.80	5.86	3.20
885	N-Slope	150	0.94	0.01	5.44	0.37	6.79	0.47	0.22	0.04	1.33	0.35	7.07	2.26
840	Summit	50	3.01	0.02	16.51	0.83	6.4	0.32	0.39	0.13	2.51	0.59	7.49	3.06
840	Summit	90	0.79	0.01	6.16	0.08	9.08	0.16	0.25	0.02	1.58	0.34	7.24	1.66
1002	W-Slope	50	6.29	0.16	30.75	6.07	5.71	1.14	0.33	0.12	1.58	0.49	5.63	2.69
875	W-Slope	150	0.59	0.01	4.43	0.52	8.8	1.04	0.07	0.02	0.45	0.13	7.90	3.21
1029	E-Slope	50	2.24	0.07	21.04	2.87	10.97	1.54	0.20	0.06	1.02	0.28	5.96	2.42
858	E-Slope	150	1.27	0.02	5.57	0.52	5.11	0.48	0.11	0.02	0.67	0.17	7.12	2.22
999	S-Slope	50	0.97	0.08	6.72	0.13	8.06	0.68	0.15	0.07	0.80	0.28	6.44	3.76
896	S-Slope	150	0.47	0.01	2.87	0.09	7.08	0.27	0.12	0.02	0.77	0.09	7.46	1.52
1048	S-Ref	50	0.61	0.04	5.19	0.12	9.88	0.69	0.08	0.03	0.45	0.11	6.76	3.03
1048	S-Ref	150	0.71	0.02	5.79	0.07	9.54	0.29	0.07	0.02	0.41	0.1	6.54	2.46

and ^{234}Th fluxes calculated based on integrated disequilibria down to 100 m. The second additional approach (ED/ED) used POC/A^{p}_{Th} values for the equilibrium depth, based on linear interpolation of the values found at 50 m and 150 m, and ^{234}Th fluxes calculated based on the equilibrium depth. The third additional approach (100/100) used POC/A^{p}_{Th} values for 100 m, based on linear interpolation of the values found at 50 and 150 m, and ^{234}Th fluxes calculated based on integrated disequilibria down to 100 m. The results of all these calculations are compiled in Fig. 12b and Table 4. Uncertainties were propagated from the ^{234}Th export estimates and POC/^{234}Th ratios and given as ±1SD and with the relative 1SD uncertainties ranging from 15% up to 37% of the mean. All four approaches result in similar

values (Fig. 12b), providing confidence in the export estimates and allowing for a comparison of the different sampling stations. In the following, the distribution of POC export fluxes will be described (Objective O2).

3.4.1. Far field

Similar to the POC and PN concentration data, the POC-flux estimates displayed a N-vs.-S difference in the far field, with values at N-Ref being more than three times higher than at S-Ref. The monthly maps of NPP as derived from the VGPM for September and October 2009 suggest there was NPP variability in the far field on the mesoscale (10–200 km) and possibly also on the submesoscale (1–10 km) (Fig. 2c and d). However, the NPP values were generally low and several studies in other subtropical and tropical ocean regions (near Hawaii: Maiti et al. (2008); at Station ALOHA: Benitez-Nelson et al. (2001), Karl et al. (1996); at BATS: Michaels and Knap (1996)) have shown that there tends to be a lack of a clear relation between primary productivity levels and export of particulate carbon. This notion is supported by the fact that in the Senghor region NPP varied by a few 10 s of percent at most while POC export at the two far-field sites differed by a factor of >3. Hence, the difference between export at N-Ref and S-Ref more likely reflects a difference in factors other than NPP that control export. As mentioned above, in October 2009, a major physical-oceanographic difference between N-Ref and S-Ref was the mesoscale horizontal current-speed gradient: at N-Ref it was high in the SW-NE direction and very weak at S-Ref and at the seamount (Fig. 2b). Higher horizontal velocity gradients increase shear and therefore also horizontal turbulence and energy dissipation. Such increased energy dissipation can lead to shear-driven aggregation of smaller, slower-settling into larger, faster-settling particles and, hence, increased export. This view is consistent with the increased ^{234}Th export fluxes that Maiti et al. (2008) found at the rim (rather than the centre) of an intense cyclonic (anticlockwise-rotating) eddy downstream of Hawaii. This aggregation mechanism is likely to have led to increased export at N-Ref, without a significant rise in NPP. At S-Ref this mechanism is weaker and NPP is also low, explaining the low observed export.

Another fluid-dynamic difference between N-Ref and S-Ref is the fact that N-Ref is located within the area where the initially downward semidiurnal internal-tide beam that emanates from the uppermost northern slope of the seamount reflects from the sea-surface for the first time, whereas S-Ref lies outside the respective surface-ocean area on the southern side of the seamount (Figs. 2a and b, 5, S3). The sea-surface reflection areas are likely to be associated with enhanced energy dissipation that could translate into increased shear-driven aggregation and export. This is also further evidence to support the notion that S-Ref is better suited as a reference for the seamount sites than N-Ref.

Finally, we include a note of caution that relates to the possible effect of atmospheric dust input. In the Introduction it was mentioned that large amounts of dust particles that are incorporated into marine-snow aggregates could lead to increased mass densities of these aggregates and, hence, higher settling speeds and POC export (e.g., Fischer et al., 2016). In the week prior to the start of the sampling for this study, a comparatively dense remotely-(MODIS-)sensed plume of dust was swept from Africa offshore and across the study region (not shown). At its most intense (probably 21–23 September 2009) the plume covered the whole study region and looked horizontally homogeneous. Only after this peak phase the atmospheric dust distribution was more heterogeneous in the form of dust filaments that were discernible until the end of September 2009. In contrast to the initial main plume with a latitudinal width of more than 1000 km, the subsequent filaments with widths of typically ~100–200 km might have caused spatial patchiness of dust input to the surface ocean. That is, it is highly unlikely that on the large scale of the main plume and the short scales of the distances between seamount sites patchy dust input played a role; however, the dust filaments could have introduced differences in dust input on scales similar to the distance between N-Ref and S-Ref. It can be concluded that, when comparing export amongst the seamount sites and between the seamount sites and S-Ref, patchy dust input is unlikely to have played a significant role.

3.4.2. POC export fluxes at the seamount

Based on the above considerations regarding the reference sites, it can now be concluded that the seamount leads to a general increase of POC export (Objective O3): on the upstream side (E-Slope) and on the sides of the seamount, looking downstream (S-Slope, N-Slope), POC export is about twice as high as at S-Ref; on the Summit and on the downstream side (W-Slope), POC export is even ~3–4 times higher than at S-Ref (Fig. 12b). In Section 3.2.2 it was argued that ^{234}Th export fluxes for N-Slope, W-Slope, S-Slope and Summit are underestimates. Such underestimates of ^{234}Th export would translate into underestimates of POC export. That is, true POC export estimates for these sites might have been even higher and deviate even more strongly from export at the upstream E-Slope site and S-Ref in the far field. Because of the shallow waters at Summit and the different positions of the other seamount sites relative to the impinging background flow and impinging barotropic tides, the slope sites and Summit will now be discussed separately, with the aim of proposing likely mechanistic scenarios that can explain their special features.

3.4.2.1. POC export fluxes at the slope sites. As mentioned above, when the far-field surface waters impinge on the seamount from the NE and pass the seamount, they are thought to pass through a tidally generated NNW-SSE screen of intensified energy dissipation and small-scale mixing. This could have two sudden effects: (1) an increased upward flux of nutrients into the euphotic zone that leads to a short pulse of primary production of new particulate matter; and (2) enhanced shear-driven aggregation of smaller, slower-settling into larger, faster-settling particles. Both effects could lead to increased export.

That such sudden nutrient input can in fact translate into brief export ‘spikes’ was shown by Buesseler et al. (1992) during the North Atlantic Bloom Experiment (NABE). Within about one day, storm-related vertical mixing led to a clearly detectable increase of nitrate concentration in the topmost water layers (see their Fig. 1). They also demonstrated that this abrupt increase was followed by an equally rapid reduction in the nitrate concentration and a concomitant drop in total ^{234}Th concentrations, suggesting that the sudden nutrient supply was rapidly converted into a moderate export flux of particulate matter.

In analogy, at Senghor, surface waters passing through the screen of enhanced mixing could have been associated with a similarly sudden and moderate increase in primary productivity and particle export. Moreover, after the waters have passed through the tidally generated mixing in the NNW-SSE screen, elevated mixing intensities (and nutrient supply into the euphotic zone) could still be sustained for several kilometers downstream of the ‘screen’ due to increased rates of energy dissipation in waters that were advected past the seamount (Gibson et al., 1993). In the NW quarter of the seamount, N-Slope is likely to be situated within the dissipation screen whereas W-Slope was most likely located downstream (to the SW) of the screen and of N-Slope. Export fluxes at W-Slope can therefore be expected to be higher than export fluxes at N-Slope; and this is what was found.

There is a biogeochemical indicator that supports the proposed scenario involving increased productivity. Production of molecular oxygen (O_2) through photosynthesis can lead to shallow subsur-

face maxima of the concentration of dissolved oxygen (DO) in the euphotic zone (Hayward, 1994). Such maxima were observed in DO profiles between ~10 m and ~50 m at almost all CTD stations across the study area (examples can be seen in Figs. 10 and 11). Depth-integration of the amount of DO in this subsurface peak above the 'background' concentration in the surface mixed layer yields an estimate of the 'excess' DO inventory in this water layer which can be interpreted as an approximate measure of photosynthetic activity.

Excess DO inventories together with the integration depths and maximum DO concentrations for each profile are given in Table 6. The highest excess DO inventories were found at station 891 (seafloor at 705 m water depth) that lies near the streamline that connects N-Slope and W-Slope, and at station 920 (2805 m water depth at the seafloor) that also lies on the NW-Slope but further away from the streamline that connects N-Slope and W-Slope (Figs. 1b and 3). At sites where repeat CTD casts were performed some temporal variability in DO inventories was displayed which may be due to the aforementioned passing internal waves. However, even if this variability is taken into account, the DO inventories on the NW slope stand out (Table 6). The high DO inventories above the NW slope, therefore, support the notion of pulsed productivity in waters passing from the northern to the western slope areas.

Unfortunately, there is no downstream station for S-Slope to scrutinise whether a signal comparable to the one of W-Slope formed above the SW side of the seamount. However, the remotely sensed NPP distribution at the time of this study showed a 'banner cloud' of slightly elevated NPP values to the SW (downstream) of the seamount (Fig. 2d) which may have resulted from a moderate seamount-driven increase of primary productivity downstream of N-Slope as well as S-Slope. This view is supported by the fact that in September 2009 there was also evidence for such a 'banner cloud' of slightly enhanced NPP on the downstream side of the seamount (then, on the eastern side: Fig. 2c).

As mentioned above, it is known that increased rates of energy dissipation can lead to enhanced shear-controlled aggregation of smaller, more slowly settling particles into larger, more rapidly settling particles (Burd and Jackson, 2009). For open-ocean waters, the upper validity threshold of this positive relationship is still not well defined, but the limited available information suggests it may be near 10^{-7}–10^{-6} m^2 s^{-3}, with net disaggregation prevailing at higher rates of energy dissipation (Alldredge et al., 1990; Berhane et al., 1997). In internal-tide beams and downstream waters of tall seamounts, rates of energy dissipation can reach up to 10^{-7}–10^{-6} m^2 s^{-3} (Lueck and Mudge, 1997; Johnston et al., 2011) (for comparison, the global average at 150 m depth is 2×10^{-8} m^2 s^{-3} (Whalen et al., 2012); and for an average trade-wind speed of 5.5 m s^{-1} the surface-ocean relation between wind speed and dissipation reported by MacKenzie and Leggett (1993) finds 10^{-8} m^2 s^{-3} for a depth of 50 m). If dissipation rates are the same in the screen at Senghor Seamount, then, particles that pass the screen and travel in downstream waters are expected to be exposed to increased rates of energy dissipation that foster aggregation into larger faster-settling particles, contributing to the increased export fluxes. Evidence for this process was found in that, at 150 m depth at W-Slope, the second-lowest POC and PN concentrations were observed in the >53 μm size fraction (only S-Ref displayed a slightly lower absolute POC concentration and a similar PN concentration). These low concentrations may well be the result of enhanced particle export due to the shear-driven net aggregation of smaller, slower-settling into larger, faster-settling particles.

3.4.2.2. POC export flux at the Summit. For the Summit, three factors need to be considered when judging the calculated POC export. (1) Because of the shallow waters on the Summit the export estimates for this station may have been affected by resuspended sediments as resuspension of sediments would lead to intensified scavenging of ^{234}Th (e.g., Turnewitsch et al., 2008). As discussed in Section 3.2.2, resuspension may have only affected the first ~10–20 m above the seafloor which means that the estimated ^{234}Th export flux would not have been strongly biased by resuspension. (2) However, moderate resuspension may have influenced the composition of particles in the >53 μm particle size fraction at 90 m that were used to calculate the POC export flux. The POC/^{234}Th ratio of 7.1 μmol dpm^{-1} for >53 μm particles from 90 m depth was the highest measured value in the near-surface waters of the study area. That is, using the POC/^{234}Th ratio from 90 m depth may have led to an *overestimation of the POC export flux*. The lower export estimate that was based on the POC/^{234}Th ratio at the equilibrium depth (75 m), with the value being derived by linear interpolation between the values from 50 m and 90 m, is probably less biased by resuspension. (3) Finally, non-negligible upward net transport of ^{234}Th into the export layer by enhanced tidally driven vertical mixing and upwelling (doming) around the

Table 6
Inventories of 'excess' dissolved molecular oxygen (DO), thickness of the excess layer, and maximum DO concentrations in the subsurface DO peaks at the bottom of the surface mixed layer.

Station	Site	Excess DO inventory (g m^{-2})	Integral height (m)	Max. DO (mg L^{-1})
801	N-Ref	76.44	17.9	195.45
803	N-Ref	99.32	13.9	199.41
808	N-Ref	93.79	11.9	199.84
885	N-Slope	136.10	24.8	206.10
902	N-Slope	129.09	13.9	199.83
905	N-Slope	112.86	20.8	199.14
911	N-Slope	56.45	9.9	197.94
891	NW-Slope	370.80	28.8	206.33
920	NW-Slope	200.23	25.0	199.79
875	W-Slope	91.42	8.9	197.12
903	W-Slope	130.84	15.9	201.08
840	Summit	142.39	17.9	196.90
844	Summit	106.58	19.8	197.98
858	E-Slope	80.30	25.9	198.31
882	SW-Slope	100.34	20.8	199.90
895	SE-Slope	60.97	8.9	194.98
896	S-Slope	95.37	12.9	198.00

summit area may have led to an *underestimation* of values for both ^{234}Th and POC export. Although the net effect of the second and third factor is unknown, it seems safe to conclude that export at the Summit is high in comparison to E-, N- and S-Slope.

This conclusion is supported by the highest POC concentration in the >53 μm particle size at 50 m depth, combined with POC concentrations in the 0.7–53 μm particle size fraction at 50 m that are low (16.5 μg L^{-1}) in comparison to the respective concentrations at stations that are more upstream (N-Slope: 30.2 μg L^{-1}; E-Slope: 21.0 μg L^{-1}), indicating conversion of smaller, more slowly settling particles into larger, more rapidly settling ones. That is, aggregation had started and resulted in enhanced export; but the process hadn't matured as much as it had done at the more downstream W-Slope where much of the >53 μm particles had been exported already. A moderate and sudden increase in the export of locally primary-produced particles may also have contributed to this overall enhancement of POC export over the Summit, as reflected by excess DO inventories that are higher in comparison to the upstream E-Slope site (Table 6).

4. Summary and conclusions

This study aimed to look for an influence of flow/topography interactions at a ~3200 m-tall seamount that reaches up to ~100 m beneath the sea surface on export of POC from the surface (the topmost ⩽100 m) into the deeper ocean. The main part of the study was carried out when both primary productivity and mesoscale productivity patchiness were low in the wider study region. The background flow was impinging on the seamount from the NE. There was no seamount-trapping of waters in the topmost ~200 m. Tidally generated internal waves are formed mainly on the upper northern and southern slopes of the seamount, probably resulting in a 'screen' of high rates of energy dissipation that runs across the seamount in the NNW-SSE direction. Hence, the background currents traversed the screen while flowing past the seamount.

The comparison between the southern reference site and seamount sites revealed what is interpreted as a detectable seamount effect on POC export: calculated POC export at the seamount sites was ~2–4 times higher than at the southern reference site. Therefore, the core hypothesis of this study that a tall seamount can trigger enhanced localised POC export is accepted. It can also be concluded that the POC export fluxes increase while the passing waters are advected from the NE towards the SW around and over the seamount, with the highest fluxes occurring on the downstream side of the seamount. This supports the view that biogeochemical and biological effects of tall seamounts in surface-ocean waters might be strongest at some (downstream) distance from, rather than centred right above, the seamount summit (e.g., Genin, 2004).

The tidally generated screen of high rates of energy dissipation that runs across the seamount is proposed to result in a combination of two main factors that led to the increased POC export above the seamount: (1) increased upward transport of nutrients into the euphotic zone, driving sudden, brief pulses of primary production of new particulate matter, followed by the particles' export into deeper waters; and (2) pulses of increased shear-driven aggregation of smaller, slower-settling into larger, faster-settling particles.

It can be speculated that a variant of the shear-based mechanism may also affect deeper seamounts and possibly even abyssal hills by controlling aggregate sinking speeds in the vicinity of the hill or seamount feature. This could relate to deposition rates and patterns of particulate matter composition on and near the feature (Durden et al., 2015; Turnewitsch et al., 2015; Morris et al., 2016) and could have implications for the concept of topographic 'stepping stones' for dispersion and migration of deep ocean fauna as well as for general drivers of spatial environmental heterogeneity in the deep sea.

Given the environmental variability in the study region, it is likely that distribution and magnitude of seamount-controlled POC export vary in space and time. Factors that contribute to this variability and might at times even overwhelm the seamount effects include seasonal variability of productivity (Lutz et al., 2007; Arístegui et al., 2009; Kiriakoulakis et al., 2009; Vilas et al., 2009), different types (clockwise, anticlockwise) of mesoscale eddies (Onken and Klein, 1991; Bashmachnikov et al., 2009), variable mineral dust inputs from the Sahara (Chiapello and Bergametti, 1995; Ratmeyer et al., 1999a,b; Brust and Waniek, 2010; Fitzsimmons et al., 2013), and high-productivity filaments and eddies extending from the Mauritania Upwelling into the Senghor Seamount area (Bory et al., 2001; Hagen, 2001; Meunier et al., 2012). What also remains unclear is how strong the biogeochemical influence of remotely generated internal tides can become when they propagate through the study area.

Keeping these caveats in mind, this study shows that, under certain conditions, there can be an effect of a tall seamount on local and possibly regional surface-ocean biogeochemistry, with tidal dynamics playing a prominent role. It can be speculated that these effects control the spatiotemporal distribution of magnitude and nutritional quality of the flux of food particles to the benthic and benthic-pelagic communities at and near the seamount. This variability may then translate into variable pelagic and benthic community distributions around the different slopes of the topography. If there is 'bottom-up' forcing on seamount biogeochemistry and biology (Rowden et al., 2010), then the nature of that forcing is also likely to vary between different seamounts, depending on where the seamount is situated within the fluid-dynamic parameter space that describes flow/topography interactions at seamounts (Turnewitsch et al., 2013).

Acknowledgements

We thank four anonymous reviewers for constructive comments that helped improve the manuscript. Samples and field data for this study were obtained during cruise M79/3 of RV Meteor and cruise 446 of RV Poseidon, and we thank the officers and crew for their contributions to this work. This study was supported through grant NE/G006415/1 of the UK's Natural Environment Research Council (NERC) and grant 669947 of the European Research Council (ERC).

Appendix A. Supplementary material

Supplementary data associated with this article can be found, in the online version, at http://dx.doi.org/10.1016/j.pocean.2016.10.009.

References

Alford, M.H., MacKinnon, J.A., Simmons, H.L., Nash, J.D., 2016. Near-inertial internal gravity waves in the ocean. Ann. Rev. Mar. Sci. 8, 95–123.

Alldredge, A.L., Granata, T.C., Gotschalk, C.C., Dickey, T.D., 1990. The physical strength of marine snow and its implications for particle disaggregation in the ocean. Limnol. Oceanogr. 35 (7), 1415–1428.

Alonso-González, I.J., Arístegui, J., Lee, C., Sanchez-Vidal, A., Calafat, A., Fabrés, J., Sangrá, P., Masqué, P., Hernández-Guerra, A., Benítez-Barrios, V., 2010. Role of slowly settling particles in the ocean carbon cycle. Geophys. Res. Lett. 37, L13608. http://dx.doi.org/10.1029/2010GL043827.

Alvarado Quiroz, N.G., Hung, C.-C., Santschi, P.H., 2006. Binding of thorium(IV) to carboxylate, phosphate and sulfate functional groups from marine exopolymeric substances (EPS). Mar. Chem. 100 (3–4), 337–353.

Arbic, B., Richman, J., Shriver, J., 2012. Global modeling of internal tides within an eddying ocean general circulation model. Oceanography 25 (2), 20–29.

Arístegui, J., Mendonça, A., Vilas, J.C., Espino, M., Polo, I., Montero, M.F., Martins, A., 2009. Plankton metabolic balance at two North Atlantic seamounts. Deep-Sea Res. Part II 56, 2646–2655.

Bashmachnikov, I., Mohn, C., Pelegrí, J.L., Martins, A., Jose, F., Machín, F., White, M., 2009. Interaction of mediterranean water eddies with Sedlo and Seine Seamounts, Subtropical Northeast Atlantic. Deep Sea Res. Part II 56, 2593–2605.

Behrenfeld, M., Falkowski, P., 1997. Photosynthetic rates derived from satellite-based chlorophyll concentration. Limnol. Oceanogr. 42 (1), 1–20.

Benitez-Nelson, C.R., Buesseler, K.O., Rutgers van der Loeff, M.M., Andrews, J., Ball, L., Crossin, G., Charette, M.A., 2001. Testing a new small-volume technique for determining thorium-234 in seawater. J. Radioanal. Nucl. Chem. 248 (3), 795–799.

Benitez-Nelson, C., Buesseler, K.O., Karl, D.M., Andrews, J., 2001. A time-series study of particulate matter export in the North Pacific Subtropical Gyre based on ^{234}Th:^{238}U disequilibrium. Deep-Sea Res. I 48, 2595–2611.

Berhane, I., Sternberg, R.W., Kineke, G.C., Milligan, T.G., Krancks, K., 1997. The variability of suspended aggregates on the Amazon Continental Shelf. Cont. Shelf Res. 17 (3), 267–285.

Bhat, S.G., Krishnaswamy, S., Lal, D., Rama, Moore, W.S., 1968. ^{234}Th/^{238}U ratios in the ocean. Earth Planet. Sci. Lett. 5, 483–491.

Bidigare, R., Benitez-Nelson, C., Leonard, C.L., Quay, P.D., Parsons, M.L., Foley, D.G., Seki, M.P., 2003. Influence of a cyclonic eddy on microheterotroph biomass and carbon export in the lee of Hawaii. Geophys. Res. Lett. 30 (6). http://dx.doi.org/10.1029/2002GL016393.

Bory, A., Jeandel, C., Leblond, N., Vangriesheim, A., Khripounoff, A., Beaufort, L., Rabouille, C., Nicolas, E., Tachikawa, K., Etcheber, H., Buat-Ménard, P., 2001. Downward particle fluxes within different productivity regimes off the Mauritanian upwelling zone (EUMELI program). Deep-Sea Res. I 48 (10), 2251–2282.

Brust, J., Waniek, J.J., 2010. Atmospheric dust contribution to deep-sea particle fluxes in the subtropical Northeast Atlantic. Deep Sea Res. I 57 (8), 988–998.

Buesseler, K., 1998. The decoupling of production and particulate export in the surface ocean. Global Biogeochem. Cycles 12 (2), 297–310.

Buesseler, K., Bacon, M.P., Cochran, J.K., Livingston, H.D., 1992. Carbon and nitrogen export during the JGOFS North Atlantic Bloom experiment estimated from ^{234}Th: ^{238}U disequilibria. Deep Sea Res. 39 (7), 1115–1137.

Buesseler, K.O., Benitez-Nelson, C.R., Moran, S.B., Burd, A., Charette, M., Cochran, J.K., Coppola, L., Fisher, N.S., Fowler, S.W., Gardner, W.D., Guo, L.D., Gustafsson, Ø., Lamborg, C., Masque, P., Miquel, J.C., Passow, U., Santschi, P.H., Savoye, N., Stewart, G., Trull, T., 2006. An assessment of particulate organic carbon to thorium-234 ratios in the ocean and their impact on the application of ^{234}Th as a POC flux proxy. Mar. Chem. 100, 213–233.

Buesseler, K.O., Lamborg, C., Cai, P., Escoube, R., Johnson, R., Pike, S., Masque, P., McGillicuddy, D., Verdeny, E., 2008. Particle fluxes associated with mesoscale eddies in the Sargasso Sea. Deep Sea Res. II 55 (10–13), 1426–1444.

Burd, A.B., Jackson, G.A., 2009. Particle aggregation. Ann. Rev. Mar. Sci. 1, 65–90.

Chapman, D., Haidvogel, D., 1992. Formation of Taylor caps over a tall isolated seamount in a stratified ocean. Geophys. Astrophys. Fluid Dyn. 64 (1–4), 31–65.

Chen, J., Edwards, R.L., Wasserburg, G.J., 1986. ^{238}U, ^{234}U and ^{232}Th in seawater. Earth Planet. Sci. Lett. 80 (3–4), 241–251.

Chiapello, I., Bergametti, G., 1995. An additional low layer transport of Sahelian and Saharan dust over the north-eastern Tropical Atlantic. Geophys. Res. Lett. 22 (23), 3191–3194.

Christiansen, B., Brand, T., Büntzow, M., Busecke, J., Coelho, R., Correia, S., Denda, A., Deniz, T., Jung, S., Kaufmann, M., Kieneke, A., Kiriakoulakis, K., Koppelmann, R., Kuhnert, J., Kwasnitschka, T., Lamont, P., Martin, B., Montgomery, J., Peine, F., Piedade, A., Reichelt, T., Rieger, V., Schmidt, A., Stahl, H., Tiedke, J., Truscheit, T., Turnewitsch, R., Unger, K., Vogel, S., Warneke-Cremer, C., 2011. Structure and Function of Seamount Ecosystems in the Cape Verde Region, Northeast Atlantic - Cruise No. M79/3 - September 24 - October 23, 2009 - Las Palmas (Spain) - Mindelo (Cape Verde). METEOR-Berichte, M79/3, 53 pp., DFG-Senatskommission für Ozeanographie, DOI: http://dx.doi.org/10.2312/cr_m79_3.

Clegg, S.L., Whitfield, M., 1990. A generalized model for the scavenging of trace metals in the open ocean - I. Particle cycling. Deep-Sea Res. 37 (5), 809–832.

Clegg, S.L., Whitfield, M., 1991. A generalized model for the scavenging of trace metals in the open ocean – II. Thorium scavenging. Deep-Sea Res. 38 (1), 91–120.

Coale, K.H., Bruland, K.W., 1985. ^{234}Th:^{238}U disequilibria within the California Current. Limnol. Oceanogr. 30 (1), 22–33.

Coale, K.H., Bruland, K.W., 1987. Oceanic stratified euphotic zone as elucidated by ^{234}Th:^{238}U disequilibria. Limnol. Oceanogr. 32 (1), 189–200.

De La Rocha, C.L., Passow, U., 2007. Factors influencing the sinking of POC and the efficiency of the biological carbon pump. Deep-Sea Res. II 54, 639–658.

Denda, A., Christiansen, B., 2014. Zooplankton distribution patterns at two seamounts in the subtropical and tropical NE Atlantic. Mar. Ecol. 35, 159–179.

Denda, A., Mohn, C., Wehrmann, H., Christiansen, B., 2016. Microzooplankton and meroplanktonic larvae at two seamounts in the subtropical and tropical NE Atlantic. J. Mar. Biol. Assoc. United Kingdom, 1–27. http://dx.doi.org/10.1017/S0025315415002192.

Dower, J., Mackas, D., 1996. "Seamount effects" in the zooplankton community near Cobb Seamount. Deep-Sea Res. I 43 (6), 837–858.

Ducklow, H., Steinberg, D., Buesseler, K.O., 2001. Upper ocean carbon export and the biological pump. Oceanography 14 (4), 50–58.

Durden, J.M., Bett, B.J., Jones, D.O.B., Huvenne, V.A.I., Ruhl, H.A., 2015. Abyssal hills - hidden source of increased habitat heterogeneity, benthic megafaunal biomass and diversity in the deep sea. Prog. Oceanogr. 137, 209–218.

Egbert, G.D., Erofeeva, S., 2002. Efficient inverse modeling of barotropic ocean tides. J. Atmos. Ocean. Technol. 19, 183–204.

Firing, E., Ranada, J., Caldwell, S., 1995. Processing ADCP Data With the CODAS Software System Version 3.1. User's Manual. Joint Institute for Marine and Atmospheric Research, University of Hawaii, USA.

Fischer, G., Romero, O., Merkel, U., Donner, B., Iversen, M., Nowald, N., Ratmeyer, V., Ruhland, G., Klann, M., Wefer, G., 2016. Deep ocean mass fluxes in the coastal upwelling off Mauritania from 1988 to 2012: variability on seasonal to decadal timescales. Biogeosciences 13 (10), 3071–3090.

Fitzsimmons, J.N., Zhang, R., Boyle, E.A., 2013. Dissolved iron in the tropical North Atlantic Ocean. Mar. Chem. 154, 87–99.

Garrett, C., Kunze, E., 2007. Internal tide generation in the deep ocean. Annu. Rev. Fluid Mech. 39 (1), 57–87.

Genin, A., 2004. Bio-physical coupling in the formation of zooplankton and fish aggregations over abrupt topographies. J. Mar. Syst. 50 (1–2), 3–20.

Gibson, C.H., Nabatov, V., Ozmidov, R., 1993. Measurements of turbulence and fossil turbulence near Ampere seamount. Dyn. Atmos. Oceans 19, 175–204.

Goldner, D.R., Chapman, D.C., 1997. Flow and particle motion induced above a tall seamount by steady and tidal background currents. Deep Sea Res. I 44 (5), 719–744.

Guo, L., Hung, C.-C., Santschi, P.H., Walsh, I.D., 2002. ^{234}Th scavenging and its relationship to acid polysaccharide abundance in the Gulf of Mexico. Mar. Chem. 78, 103–119.

Hagen, E., 2001. Northwest African upwelling scenario. Oceanol. Acta 24 (S), S113–S128.

Hanel, R., John, H.-C., Meyer-Klaeden, O., Piatkowski, U., 2010. Larval fish abundance, composition and distribution at Senghor Seamount (Cape Verde Islands). J. Plankton Res. 32 (11), 1541–1556.

Hayward, T.L., 1994. The shallow oxygen maximum layer and primary production. Deep-Sea Res. I 41 (3), 559–574.

Hummon, J., Firing, E., 2003. A direct comparison of two RDI shipboard ADCPs: a 75-KHz Ocean surveyor and a 150-kHz narrow band. J. Atmos. Ocean. Technol. 20, 872–888.

Johnston, T.M.S., Rudnick, D.L., Carter, G.S., Todd, R.E., Cole, S.T., 2011. Internal tidal beams and mixing near Monterey Bay. J. Geophys. Res. 116, C03017.

Karl, D.M., Christian, J.R., Dore, J.E., Hebel, D.V., Letelier, R.M., Tupas, L.M., Winn, C.D., 1996. Seasonal and interannual variability in primary production and particle flux at Station ALOHA. Deep-Sea Res. II 43, 539–568.

Kiriakoulakis, K., Vilas, J.C., Blackbird, S.J., Arístegui, J., Wolff, G.A., 2009. Seamounts and organic matter—Is there an effect? The case of Sedlo and Seine seamounts, Part 2. Composition of suspended particulate organic matter. Deep Sea Res. II 56 (25), 2631–2645.

Lamb, K.G., 2004. Nonlinear interaction among internal wave beams generated by tidal flow over supercritical topography. Geophys. Res. Lett. 31, L09313. doi:09310.01029/02003GL019393.

Lampitt, R.S., Boorman, B., Brown, L., Lucas, M., Salter, I., Sanders, R., Saw, K., Seeyave, S., Thomalla, S.J., Turnewitsch, R., 2008. Particle export from the euphotic zone: estimates using a novel drifting sediment trap, ^{234}Th and new production. Deep-Sea Res. I 55 (11), 1484–1502.

Lathuilière, C., Echevin, V., Lévy, M., 2008. Seasonal and intraseasonal surface chlorophyll-*a* variability along the northwest African coast. J. Geophys. Res. 113 (C5), C05007. http://dx.doi.org/10.1029/2007JC004433.

Lavelle, J.W., Mohn, C., 2010. Motion, commotion, and biophysical connections at deep ocean seamounts. Oceanography 23 (1), 90–103.

Lázaro, C., Fernandes, M.J., Santos, A.M.P., Oliveira, P., 2005. Seasonal and interannual variability of surface circulation in the Cape Verde region from 8 years of merged T/P and ERS-2 altimeter data. Remote Sens. Environ. 98 (1), 45–62.

Legg, S., Huijts, K.M.H., 2006. Preliminary simulations of internal waves and mixing generated by finite amplitude tidal flow over isolated topography. Deep-Sea Res. II 53 (1–2), 140–156.

Legg, S., Klymak, J., 2008. Internal hydraulic jumps and overturning generated by tidal flow over a tall steep ridge. J. Phys. Oceanogr. 38 (9), 1949–1964.

Le Moigne, F.A.C., Villa-Alfagem, M., Sanders, R.J., Marsay, C., Henson, S., García-Tenorio, R., 2013. Export of organic carbon and biominerals derived from ^{234}Th and ^{210}Po at the Porcupine Abyssal Plain. Deep-Sea Res. I 72, 88–101.

Lueck, R.G., Mudge, T.D., 1997. Topographically induced mixing around a shallow seamount. Science 276, 1831–1833.

Lutz, M.J., Caldeira, K., Dunbar, R.B., Behrenfeld, M.J., 2007. Seasonal rhythms of net primary production and particulate organic carbon flux to depth describe the efficiency of biological pump in the global ocean. J. Geophys. Res. 112 (C10), C10011. http://dx.doi.org/10.1029/2006JC003706.

Luyten, J., Pedlosky, J., Stommel, H., 1983. The ventilated thermocline. J. Phys. Oceanogr. 13, 292–309.

MacKenzie, B.R., Leggett, W.C., 1993. Wind-based models for estimating the dissipation rates of turbulent energy in aquatic environments: empirical comparisons. Mar. Ecol. Prog. Ser. 94, 207–216.

Maiti, K., Buesseler, K.O., Pike, S.M., Benitez-Nelson, C., Cai, P., Chen, W., Cochran, K., Dai, M., Dehairs, F., Gasser, B., Kelly, R.P., Masque, P., Miller, L., Miquel, J.C., Moran, S.B., Morris, P.J., Peine, F., Planchon, F., Renfro, A.A., Rutgers van der Loeff, M., Santschi, P., Turnewitsch, R., Waples, J.T., Xu, C., 2012. Intercalibration studies of short-lived thorium-234 in the water column and marine particles. Limnol. Oceanogr.: Methods 10, 631–644.

Maiti, K., Benitez-Nelson, C.R., Bidigare, R., 2008. The influence of a mature cyclonic eddy on particle export. Deep Sea Res. II 55, 1445–1460.

Marshall, J., Adcroft, A., Hill, C., Perelman, L., Heisey, C., 1997. A finite-volume, incompressible Navier Stokes model for studies of the ocean on parallel computers. J. Geophys. Res. 102 (C3), 5753–5766.

Martínez-Marrero, A., Rodríguez-Santana, A., Hernández-Guerra, A., Fraile-Nuez, E., López-Laatzen, F., Vélez-Belchí, P., Parrilla, G., 2008. Distribution of water masses and diapycnal mixing in the Cape Verde Frontal Zone. Geophys. Res. Lett. 35 (7), L07609. http://dx.doi.org/10.1029/2008GL033229.

McCave, I.N., 1975. Vertical flux of particles in the ocean. Deep-Sea Res. 22, 491–502.

Meunier, T., Barton, E.D., Barreiro, B., Torres, R., 2012. Upwelling filaments off Cap Blanc: interaction of the NW African upwelling current and the Cape Verde frontal zone eddy field? J. Geophys. Res. 117 (C8), 1–18.

Michaels, A.F., Knap, A.H., 1996. Overview of the US JGOFS Bermuda Atlantic Time series Study and the Hydrostation S program. Deep-Sea Res. II 43 (2–3), 157–198.

Mittelstaedt, E., 1983. The upwelling area off Northwest Africa—a description of phenomena related to coastal upwelling. Prog. Oceanogr. 12, 307–331.

Mohn, C., White, M., 2010. Seamounts in a restless ocean: response of passive tracers to sub-tidal flow variability. Geophys. Res. Lett. 37 (15), 1–5.

Mohn, C., Erofeeva, S., Turnewitsch, R., Christiansen, B., White, M., 2013. Tidal and residual currents over abrupt deep-sea topography based on shipboard ADCP data and tidal model solutions for three popular bathymetry grids. Ocean Dyn. 63 (2–3), 195–208.

Morris, K.J., Bett, B.J., Durden, J.M., Benoist, N.M.A., Huvenne, V.A.I., Jones, D.O.B., Robert, K., Ichino, M.C., Wolff, G.A., Ruhl, H.A., 2016. Landscape-scale spatial heterogeneity in phytodetrital cover and megafauna biomass in the abyss links to modest topographic variation. Sci. Reports 6, 34080. http://dx.doi.org/10.1038/srep34080.

Morris, P.J., Sanders, R., Turnewitsch, R., Thomalla, S., 2007. ^{234}Th-derived particulate organic carbon export from an island-induced phytoplankton bloom in the Southern Ocean. Deep-Sea Res. II 54, 2208–2232.

Mouriño, B., Fernández, E., Serret, P., Harbour, D., Sinha, B., Pingree, R., 2001. Variability and seasonality of physical and biological fields at the Great Meteor Tablemount (subtropical NE Atlantic). Oceanol. Acta 24 (2), 1–20.

Müller, B., Siedler, G., 1992. Multi-year current time series in the eastern North Atlantic Ocean. J. Mar. Res. 50, 63–98.

Mullineau, L., Mills, S., 1997. A test of the larval retention hypothesis in seamount-generated flows. Deep Sea Res. I 44 (5), 745–770.

Ohde, T., Siegel, H., 2010. Biological response to coastal upwelling and dust deposition in the area off Northwest Africa. Cont. Shelf Res. 30 (9), 1108–1119.

Onken, R., Klein, B., 1991. A model of baroclinic instability and waves between the ventilated gyre and the shadow zone of the North Atlantic Ocean. J. Phys. Oceanogr. 21, 53–67.

Owens, S.A., Buesseler, K.O., Sims, K.W.W., 2011. Re-evaluating the ^{238}U-salinity relationship in seawater: Implications for the ^{238}U–^{234}Th disequilibrium method. Mar. Chem. 127 (1–4), 31–39.

Owens, S.A., Pike, S., Buesseler, K.O., 2015. Thorium-234 as a tracer of particle dynamics and upper ocean export in the Atlantic Ocean. Deep-Sea Res. II 116, 42–59.

Passow, U., Murray, J.W., Balistrieri, L., Alldredge, A.L., 2006. Organic carbon to ^{234}Th ratios of marine organic matter. Mar. Chem. 100 (3–4), 323–336.

Pastor, M.V., Pelegrí, J.L., Hernández-Guerra, A., Fonta, J., Salata, J., Emelianov, M., 2008. Water and nutrient fluxes off Northwest Africa. Cont. Shelf Res. 28 (7), 915–936.

Peine, F., Turnewitsch, R., Mohn, C., Reichelt, T., Springer, B., Kaufmann, M., 2009. The importance of tides for sediment dynamics in the deep sea - Evidence from the particulate-matter tracer ^{234}Th in deep-sea environments with different tidal forcing. Deep Sea Res. I 56 (7), 1182–1202.

Ratmeyer, V., Balzer, W., Bergametti, G., Chiapello, I., Fischer, G., Wyputta, U., 1999a. Seasonal impact of mineral dust on deep-ocean particle flux in the eastern subtropical Atlantic Ocean. Mar. Geol. 159 (1–4), 241–252.

Ratmeyer, V., Fischer, G., Wefer, G., 1999b. Lithogenic particle fluxes and grain size distributions in the deep ocean off northwest Africa: implications for seasonal changes of aeolian dust input and downward. Deep-Sea Res. 46, 1289–1337.

Resplandy, L., Martin, A.P., LeMoigne, F., Martin, P., Aquilina, A., Mémery, L., Lévy, M., Sanders, R., 2012. How does dynamical spatial variability impact ^{234}Th-derived estimates of organic export? Deep-Sea Res. I 68, 24–45.

Rodriguez y Baena, A.M., Metian, M., Teyssié, J.-L., De Broyer, C., Warnau, M., 2006. Experimental evidence for ^{234}Th bioaccumulation in three Antarctic crustaceans: Potential implications for particle flux studies. Mar. Chem. 100, 354–365.

Rogers, 1994. The biology of seamounts. Adv. Mar. Biol. 30, 305–350.

Rowden, A.A., Dower, J.F., Schlacher, T.A., Consalvey, M., Clark, M.R., 2010. Paradigms in seamount ecology: fact, fiction and future. Mar. Ecol. 31 (S1), 226–241.

Rutgers van der Loeff, M., Sarin, M.M., Baskaran, M., Benitez-Nelson, C., Buesseler, K. O., Charette, M., Dai, M., Gustafsson, Ö., Masque, P., Morris, P.J., Orlandini, K., Rodriguez y Baena, A., Savoye, N., Schmidt, S., Turnewitsch, R., Vöge, I., Waples, J.T., 2006. A review of present techniques and methodological advances in analyzing ^{234}Th in aquatic systems. Mar. Chem. 100 (3-4), 190–212.

Rutgers van der Loeff, M.M., Moore, W.S., 1999. Determination of natural radioactive tracers. In: Grasshoff, K., Kremling, K., Ehrhardt, M. (Eds.), Methods of Seawater Analysis. Wiley-VCH, Weinheim, pp. 365–397.

Santschi, P.H., Murray, J.W., Baskaran, M., Benitez-Nelson, C.R., Guo, L.D., Hung, C.-C., Lamborg, C., Moran, S.B., Passow, U., Roy-Barman, M., 2006. Thorium speciation in seawater. Mar. Chem. 100 (3–4), 250–268.

Savoye, N., Benitez-Nelson, C., Burd, A.B., Cochran, J.K., Charette, M., Buesseler, K.O., Jackson, G.A., Roy-Barman, M., Schmidt, S., Elskens, M., 2006. ^{234}Th sorption and export models in the water column: a review. Mar. Chem. 100 (3–4), 234–249.

Schlitzer, R., 2002. Interactive analysis and visualization of geoscience data with Ocean Data View. Comput. Geosci. 28 (10), 1211–1218.

Siedler, G., Paul, U., 1991. Barotropic and baroclinic tidal currents in the eastern basins of the North Atlantic. J. Geophys. Res. 96 (C12), 22259–22271.

Siedler, G., Zangenberg, N., 1992. Seasonal changes in the tropical Atlantic circulation: observation and simulation of the Guinea Dome. J. Geophys. Res. 97 (C1), 703–715.

Stramma, L., Siedler, G., 1988. Seasonal changes in the North-Atlantic sub-tropical gyre. J. Geophys. Res. 93 (C7), 8111–8118.

Stramma, L., Brandt, P., Schafstall, J., Schott, F., Fischer, J., Körtzinger, A., 2008. Oxygen minimum zone in the North Atlantic south and east of the Cape Verde Islands. J. Geophys. Res. 113, 1–15.

Troupin, C., Mason, E., Beckers, J.-M., Sangra, P., 2012. Generation of the Cape Ghir upwelling filament: a numerical study. Ocean Model. 41, 1–15.

Turnewitsch, R., Falahat, S., Nycander, J., Dale, A., Scott, R.B., Furnival, D., 2013. Deep-sea fluid and sediment dynamics—influence of hill- to seamount-scale seafloor topography. Earth Sci. Rev. 127, 203–241.

Turnewitsch, R., Springer, B.M., Kiriakoulakis, K., Vilas, J.C., Arístegui, J., Wolff, G., Peine, F., Werk, S., Graf, G., Waniek, J.J., 2007. Determination of particulate organic carbon (POC) in seawater: the relative methodological importance of artificial gains and losses in two glass-fiber-filter-based techniques. Mar. Chem. 105 (3–4), 208–228.

Turnewitsch, R., Reyss, J.-L., Nycander, J., Waniek, J.J., Lampitt, R.S., 2008. Internal tides and sediment dynamics in the deep sea—Evidence from radioactive ^{234}Th/^{238}U disequilibria. Deep-Sea Res. I 55 (12), 1727–1747.

Turnewitsch, R., Springer, B., 2001. Do bottom mixed layers influence ^{234}Th dynamics in the abyssal near-bottom water column? Deep-Sea Res. I 48, 1279–1307.

Turnewitsch, R., Lahajnar, N., Haeckel, M., Christiansen, B., 2015. An abyssal hill fractionates organic and inorganic matter in deep-sea surface sediments. Geophys. Res. Lett. 42. http://dx.doi.org/10.1002/2015GL065658.

Vangriesheim, A., Bournot-Marec, C., Fontan, A., 2003. Flow variability near the Cape Verde frontal zone (subtropical Atlantic Ocean). Oceanol. Acta 26, 149–159.

Verdeny, E., Masqué, P., Maiti, K., Garcia-Orellana, J., Bruach, J.M., Mahaffey, C., Benitez-Nelson, C.R., 2008. Particle export within cyclonic Hawaiian lee eddies derived from Pb-210-Po-210 disequilibrium. Deep Sea Res. II 55 (10–13), 1461–1472.

Vilas, J.C., Arístegui, J., Kiriakoulakis, K., Wolff, G.A., Espino, M., Polo, I., Montero, M. F., Mendonça, A., 2009. Seamounts and organic matter - Is there an effect? The case of Sedlo and Seine Seamounts: Part 1. Distributions of dissolved and particulate organic matter. Deep-Sea Res. II 56, 2618–2630.

Waterhouse, A.F., MacKinnon, J.A., Nash, J.D., Alford, M.H., Kunze, E., Simmons, H.L., Polzin, K.L., St Laurent, L.C., Sun, O.M., Pinkel, R., Talley, L.D., Whalen, C.B., Huussen, T.N., Carter, G.S., Fer, I., Waterman, S., Garabato, A.C.N., Sanford, T.B., Lee, C.M., 2014. Global patterns of diapycnal mixing from measurements of the turbulent dissipation rate. J. Phys. Oceanogr. 44 (7), 1854–1872.

Watling, L., Guinotte, J., Clark, M.R., Smith, C.R., 2013. A proposed biogeography of the deep ocean floor. Prog. Oceanogr. 111, 91–112.

Wessel, P., Sandwell, D., Kim, S., 2010. The global seamount census. Oceanography 23 (1), 24–33.

Whalen, C.B., Talley, L.D., MacKinnon, J.A., 2012. Spatial and temporal variability of global ocean mixing inferred from Argo profiles. Geophys. Res. Lett. 39, L18612. http://dx.doi.org/10.1029/2012GL053196.

White, M., Mohn, C., 2004. Seamounts: a review of physical processes and their influence on the seamount ecosystem. Oasis Report: <http://epic.awi.de/37314/17/OASIS_Oceanography.pdf>.

Yamamouro, M., Kayanne, H., 1995. Rapid direct determination of organic carbon and nitrogen in carbonate-bearing sediments with a Yanaco MT-5 CHN analyser. Limnol. Oceanogr. 40, 1001–1005.

Zenk, W., Klein, B., Schröder, M., 1991. Cape Verde frontal zone. Deep-Sea Res. 38 (S1), S505–S530.